

**Discrete inclusion models for reinforced composites  
Comparative performance analysis and modeling challenges**

Goudarzi, M.; Simone, A.

**DOI**

[10.1016/j.cma.2019.06.026](https://doi.org/10.1016/j.cma.2019.06.026)

**Publication date**

2019

**Document Version**

Final published version

**Published in**

Computer Methods in Applied Mechanics and Engineering

**Citation (APA)**

Goudarzi, M., & Simone, A. (2019). Discrete inclusion models for reinforced composites: Comparative performance analysis and modeling challenges. *Computer Methods in Applied Mechanics and Engineering*, 355, 535-557. <https://doi.org/10.1016/j.cma.2019.06.026>

**Important note**

To cite this publication, please use the final published version (if applicable).  
Please check the document version above.

**Copyright**

Other than for strictly personal use, it is not permitted to download, forward or distribute the text or part of it, without the consent of the author(s) and/or copyright holder(s), unless the work is under an open content license such as Creative Commons.

**Takedown policy**

Please contact us and provide details if you believe this document breaches copyrights.  
We will remove access to the work immediately and investigate your claim.

# Discrete inclusion models for reinforced composites: Comparative performance analysis and modeling challenges

M. Goudarzi<sup>a,\*</sup>, A. Simone<sup>a,b</sup>

<sup>a</sup> Faculty of Civil Engineering and Geosciences, Delft University of Technology, Delft, The Netherlands

<sup>b</sup> Department of Industrial Engineering, University of Padova, Padua, Italy

Received 20 March 2019; received in revised form 14 June 2019; accepted 17 June 2019

Available online 5 July 2019

## Highlights

- Embedded reinforcement models are reviewed.
- Classical embedded reinforcement models show spurious oscillations in slip profiles.
- Improved versions of classical models are proposed.
- Weak discontinuity and order/regularity extension effectively reduce oscillations.

## Abstract

We report the results of a comparative analysis of mesh independent discrete inclusion models and point out some shortcomings of classical approaches in the approximation of the strain field across an inclusion (artificial continuity) and the slip profile along an inclusion (oscillatory behavior). We also present novel embedded reinforcement models based on partition of unity enrichment strategies, adaptive  $h$ -refinement, and order/regularity extensions. These novel models are assessed by means of mesh convergence studies and it is shown that they improve the quality of the solution by significantly decreasing local spurious oscillations in the slip profile along an inclusion.

© 2019 Elsevier B.V. All rights reserved.

*Keywords:* Fiber-reinforced composite; Platelet inclusion; Embedded reinforcement; Non-smooth slip profile

## 1. Introduction

A reliable prediction of the mechanical behavior of a reinforced composite can only be obtained with the aid of modeling approaches that describe geometry and deformations of reinforcing agents with adequate precision and are equipped with appropriate constitutive models. With reference to high aspect ratio inclusions such as platelets or fibers (or, equivalently, rebars), the most accurate modeling approach for this task is the finite element method (FEM) with conformal meshing of individual inclusions, an approach that might be (prohibitively) expensive if done at an adequate resolution level [1, Figure 2]. Embedded reinforcement models, lifting the meshing constraints typical of classical FEM approaches, are a viable alternative to conformal FEM discretizations. In this contribution

\* Corresponding author.

E-mail addresses: [m.goudarzi@tudelft.nl](mailto:m.goudarzi@tudelft.nl) (M. Goudarzi), [angelo.simone@unipd.it](mailto:angelo.simone@unipd.it), [a.simone@tudelft.nl](mailto:a.simone@tudelft.nl) (A. Simone).

we compare the performance of existing and novel embedded reinforcement models while highlighting some of their limitations and suggesting strategies to improve their performance. Although in the examples we make reference to thin (high aspect ratio) platelet inclusions in a two-dimensional setting for convenience, the results of this study hold also for high aspect ratio fibers as both inclusions can be approximated as one dimensional objects under planar conditions. Fibers and platelets are referred to as inclusions throughout the paper when discussing general concepts.

Fibers or platelet inclusions as reinforcing agents can be modeled in several manners by borrowing approaches originally developed for rebars in reinforced concrete structures or by means of dedicated approaches [2–13]. A simplistic classification can be into two broad categories: implicit and explicit approaches. In the first approach, also called continuous approach, the collective effect of the inclusions on the response of the composite is taken into account in an indirect manner by means of suitable modifications to the constitutive model and material properties of the composite, which is seen as a continuum with homogeneous properties; in the second approach, also known as the discrete approach, each inclusion is directly taken into account either using solid finite elements or simplified dimensionally reduced discretizations. In this study we focus on the latter.

In explicit inclusion models we distinguish between conformal and non-conformal approaches, depending on the way the inclusion is discretized with respect to the discretization of the matrix material. Explicit approaches can then be classified according to the fidelity of the discretization with respect to the actual geometry. In the most accurate approaches, geometrical details of the inclusions are discretized using the standard conformal finite element method with solid elements [1,3,14,15]. Similar studies have been conducted for high aspect ratio platelet clay inclusions, represented by means of two-dimensional [16] and three-dimensional [17] finite element models. Although very accurate, explicit inclusion models suffer from costly mesh generation procedures, hence making the study of composites with a large number of inclusions difficult. An exception is the conformal method proposed by Soghrati et al. [15] in which background elements cut by an interface are morphed to generate a conformal discretization, thus simplifying the meshing procedure and reducing its cost. Based on advances in the use of enriched basis functions in the finite element method [18], it is possible to describe intra-element discontinuous fields, thus relaxing the mesh conformity restrictions of classical FEM approaches. Such an approach has been pursued by Moës et al. [19] who adopted a material discontinuity enrichment function to represent the intra-element perfectly bonded interface between matrix and inclusion. Related approaches include the work of Omerović and Fries [20] and the interface-enriched generalized finite element method (IGFEM) [21,22].

Such methods however are not easily applicable to dense inclusion distributions and may require extremely fine discretizations, especially for high aspect ratio fiber inclusions such as rebars, thin fibers, or carbon nanotubes. In these cases, the geometrical configuration of the inclusion allows considerable modeling simplifications as it can be represented as a one-dimensional object in a finite element discretization, similar to the approach employed in early finite element analyses of reinforced concrete structures. A further simplification originates from the common understanding that in composites with high aspect ratio fibers the axial deformation contribution to the strain energy is significantly larger compared to that of other deformation mechanisms, thus allowing to represent a fiber by means of kinematic quantities related to the axial deformation only. Phillips and Zienkiewicz [23] were the first to consider these simplifications in a computational study of reinforced concrete by employing axially-deformable bar elements to represent rebars. In their approach, rebars are perfectly bonded and discretized in a non-conformal manner with respect to the matrix material mesh. Such non-conformal approaches are known as embedded reinforcement models.

The idea of adopting explicit degrees of freedom (DOFs) to represent the relative tangential displacement between inclusion and matrix (slip) was first employed by Balakrishnan and Murray [2]. This approach, which will be referred to as embedded reinforcement model with slip (ERS model) in this paper, can be understood as a generalization of the embedded reinforcement model proposed by Phillips and Zienkiewicz [23] to imperfect interfaces and has been successfully applied to numerous engineering problems [24–28].

One-dimensional fiber inclusions in a two-dimensional setting can also be represented by means of a partition of unity enrichment strategy. The approach proposed by Radtke et al. [29] enriches the nodes of the elements crossed by a fiber inclusion with DOFs representing the relative displacement between inclusion and matrix (including normal and tangential components). Although the approach allows to incorporate a priori known enrichment functions to improve the convergence rate of the numerical solution, the corresponding enrichment scheme is relatively expensive, especially its extension to three-dimensions, as it effectively doubles the number of elemental DOFs when an element is crossed by a fiber. This is in contrast with the ERS model, which only requires slip DOFs to be placed

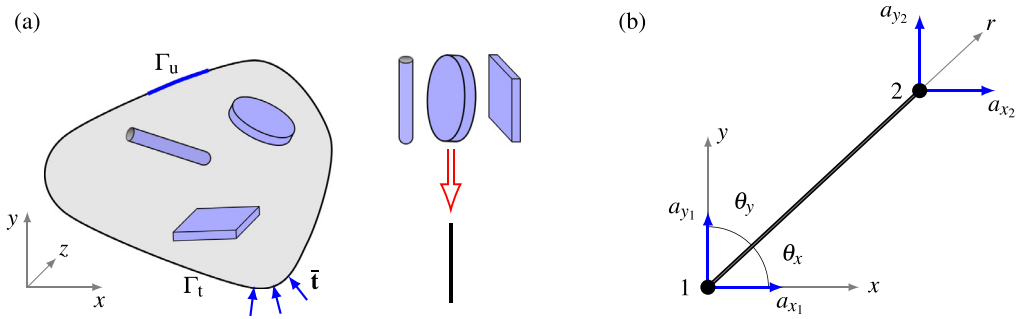


**Fig. 1.** (a) Schematic of a composite with several types of high aspect ratio inclusions (these inclusions can be described as line inclusions). (b) Local coordinate system for an arbitrary two-dimensional inclusion segment.

at matrix-fiber intersection points. A related XFEM based approach was proposed by Pike and Oskay [30] who were the first to consider both weak and strong discontinuity enrichments (referred to as fiber and debonding enrichments) to represent the effect of a debonding fiber in the matrix displacement field. As shown in Section 2.2, these two enrichments are necessary as a fiber inclusion introduces weak and strong discontinuities in the displacement field of the matrix material. Both approaches [29,30] use the partition of unity enrichment strategy and therefore require a distributed enrichment scheme (all nodes of elements crossed by a fiber are enriched, with one extra set of DOFs for enrichment). In contrast, ERS models (Section 3) require dedicated DOFs along the fiber itself but cannot properly represent the weak discontinuity (Section 4.1) because of the assumptions in the displacement field (*i.e.*, artificial continuity of the strain field in the matrix across an inclusion). Incorporating such discontinuities adds to the complexity in terms of implementation as it requires a dedicated independent conformal integration mesh similar to that used by Pike and Oskay [30]. Also, a direct three-dimensional extension is not straightforward (Pike and Oskay [31] have incorporated short fibers as deformable rectangular planar inclusions).

Among the discrete approaches described above, the techniques with an exact geometrical representation of the inclusions are, obviously, the most accurate. Accuracy, however, comes with high computational costs even for limited number of inclusions. Dimensionally reduced approaches of the ERS type combine adequate accuracy with numerical efficiency. Their classical version and several novel formulations designed to improve specific characteristics are assessed in Sections 4 and 5. It is shown that some formulations are more effective than others in addressing the occurrence of oscillations in the slip profile but none can remove them.

## 2. Governing equations

Under the assumption of small deformations, the principle of virtual work for the two-phase reinforced composite occupying the volume  $\Omega$  in Fig. 1a reads

$$\int_{\Omega} \boldsymbol{\sigma} : \nabla^s \delta \mathbf{u} \, d\Omega + \int_{\Gamma_{\text{int}}} \mathbf{t}_{\text{int}} \cdot \delta \mathbf{w} \, d\Gamma_{\text{int}} - \int_{\Gamma_t} \bar{\mathbf{t}} \cdot \delta \mathbf{u} \, d\Gamma_t = 0 \tag{1}$$

for every virtual displacement field  $\delta \mathbf{u}$ , and with the displacement gap vector  $\mathbf{w}$  a function of the displacement vector  $\mathbf{u}$ . In (1), we have neglected body forces,  $\boldsymbol{\sigma}$  is the stress tensor, and  $\nabla^s$  is the symmetric gradient operator. The first integral has not been divided yet into matrix and inclusion components as they obey the same governing equations. Since the inclusion is not perfectly bonded, the second term in (1) represents the virtual mechanical work across the matrix-inclusion interface  $\Gamma_{\text{int}}$  due to the interface tractions  $\mathbf{t}_{\text{int}}$  and the corresponding matrix-inclusion displacement gap vector  $\mathbf{w}$ . The last term represents the work done by the external tractions  $\bar{\mathbf{t}}$  on the external surface  $\Gamma_t$ .

### 2.1. Discretization using conformal FEM

We now describe a reference model in the context of the standard finite element method and solve a benchmark problem that will also be used later with the discretization techniques discussed in Section 3. The domain  $\Omega$  is subdivided into matrix and inclusion subdomains ( $\bar{\Omega} = \bar{\Omega}_m \cup \bar{\Omega}_i$ , with subscripts *i* and *m* indicating inclusion and

matrix contributions, respectively). This reference model is based on the model by Ngo and Scordelis [32]. Here, the discretized one-dimensional inclusion  $\Omega_i$  is linked to the underlying discretized matrix material  $\Omega_m$  by an interface element that allows a relative displacement between inclusion and matrix. The inclusion has to be understood as being superimposed on the matrix rather than being surrounded by it. A conformal discretization for matrix and inclusion is assumed where standard four-node quadrilateral (Q4) or three-node triangular (T3) finite elements are used for the matrix, and a one-dimensional discretization, described in the next section, is employed for inclusion and corresponding matrix-inclusion interface contributions (the second term in (1)). The last term is discretized following standard procedures.

*Inclusion.* The conformal discretization approach can be used for fiber based composites in two and three dimensions and for platelet inclusions in a two-dimensional setup (under the plane strain assumption). All the examples discussed in this paper make reference to platelets; we thus assume that inclusions are in the shape of high aspect ratio platelets and are discretized by means of conventional two node truss elements (assuming therefore plane strain conditions in all the examples). Consequently, each inclusion element is characterized by a one-dimensional displacement field along its axis. The stiffness matrix in the global  $xy$  coordinate system for an inclusion element of length  $L$  is then given by

$$\mathbf{K}_i = \frac{\bar{E}_i A_i}{L} \begin{pmatrix} l^2 & lm & -l^2 & -lm \\ lm & m^2 & -lm & -m^2 \\ -l^2 & -lm & l^2 & lm \\ -lm & -m^2 & lm & m^2 \end{pmatrix}, \quad \text{with } l = \frac{x_2 - x_1}{L}, \quad m = \frac{y_2 - y_1}{L}, \quad (2)$$

where  $\bar{E}_i = E_i - E_m$  is the effective stiffness of the inclusion with  $E_m$  and  $E_i$  the Young's moduli of matrix and inclusion, respectively. The inclusion effective stiffness has been introduced to remove the contribution of the matrix material related to the inclusion region. The coordinates of an inclusion segment endpoints (points 1 and 2 in Figs. 1a and 2) are  $(x_1, y_1)$  and  $(x_2, y_2)$ , and its cross sectional area is  $A_i = d_i t_i$ , with  $d_i$  and  $t_i = 1 \mu\text{m}$  the in-plane and out-of-plane widths of the inclusion segment, respectively.

*Inclusion–matrix interface.* The relative displacement between an inclusion and the underlying matrix can be represented with the aid of conventional zero-thickness conformal interface elements (Fig. 2a) that are equivalent to the linkage elements proposed by Ngo and Scordelis [32]. Since the discretization of the matrix material is not modified when an inclusion is superimposed on it, the continuity of the underlying matrix displacement field is not influenced. The interface gap vector (this is the relative displacement between interface and matrix) in the coordinate system local to the inclusion is discretized by

$$\mathbf{w} = \mathbf{R} \mathbf{N}_{\text{int}} \mathbf{d}_{\text{int}}, \quad (3)$$

where  $\mathbf{R}$  is the conventional global-to-local rotation matrix, and the interface shape function matrix and interface nodal displacement vector are defined as

$$\mathbf{N}_{\text{int}} = \begin{bmatrix} N_{i1} & 0 & N_{i2} & 0 & -N_{m1} & 0 & -N_{m2} & 0 \\ 0 & N_{i1} & 0 & N_{i2} & 0 & -N_{m1} & 0 & -N_{m2} \end{bmatrix} \quad (4)$$

and

$$\mathbf{d}_{\text{int}} = [\mathbf{u}_{i1} \quad \mathbf{u}_{i2} \quad \mathbf{u}_{m1} \quad \mathbf{u}_{m2}]^T, \quad (5)$$

respectively, where subscripts 1 and 2 indicate corresponding inclusion endpoints,  $N$  indicates one-dimensional shape functions (along the inclusion segment and along the edge of the matrix element next to it), and  $\mathbf{u}$  are displacement vectors in the global coordinate system.

Substituting (3) into the second term in (1) and following standard procedures yield the interface stiffness contribution

$$\mathbf{K}_{\text{int}} = C_i \int_L \mathbf{N}_{\text{int}}^T \mathbf{R}^T \mathbf{D}_b \mathbf{R} \mathbf{N}_{\text{int}} dr \quad (6)$$

in which  $L$  is the length of the inclusion–matrix interface element (known also as bond element and with length equal to that of the inclusion element),  $C_i = 2 t_i$  is a factor, together with  $L$ , taking into account the actual surface of the inclusion–matrix interface region, and  $r$  is the local coordinate along the bond element. A linear traction

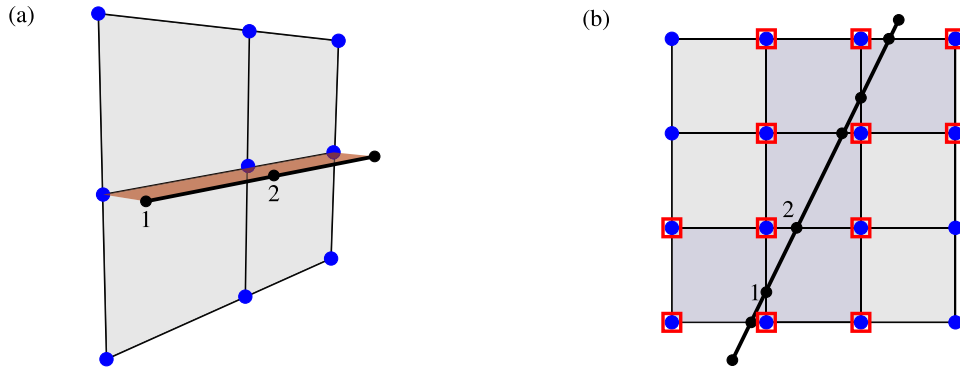


**Fig. 2.** (a) Schematic of the reference composite model with conformal discretization of the inclusion. Blue and black dots represent matrix and inclusion nodes, respectively. Zero-thickness interface elements (red shaded region) are placed between inclusion (solid black line) and matrix elements. Strain discontinuity is naturally achieved because of the standard FEM displacement field approximation. (b) An arbitrarily-located inclusion discretized with the ERS model (Section 3.1.1); strain discontinuity is achieved by enriching the nodes of the elements crossed by the inclusion (marked with a red squares) with a weak discontinuity enrichment function as discussed in Section 3.2. (For interpretation of the references to color in this figure legend, the reader is referred to the web version of this article.)

separation law is considered ( $\mathbf{t}_{\text{int}} = \mathbf{D}_b \mathbf{w}$ ), with the elastic interface constitutive matrix  $\mathbf{D}_b = \text{diag}(K_{bt}, K_{bn})$ , where the constants  $K_{bt}$  and  $K_{bn}$  represent the stiffness of the interface in the directions tangential and normal to the inclusion axis, respectively. In this conformal model, we only allow the relative displacement in the tangential direction (slip) by constraining the normal relative displacement by using large values of the interface normal stiffness  $K_{bn}$ . Preliminary analyses of the global stiffness matrix for the case of one inclusion indicate that its condition number does not significantly change by changing the interface constants. The condition number is in any case higher than the original system without inclusion, and this can be attributed to the augmented structure of the stiffness matrix when inclusions are considered. In these situations, a direct numerical solver is to be preferred; iterative solvers could also be used, but require appropriate preconditioners.

## 2.2. Benchmark problem

The benchmark problem discussed in this section is used to evaluate the performance of the numerical models presented throughout the paper. Fig. 3 shows geometry and boundary conditions of a  $4 \mu\text{m} \times 4 \mu\text{m}$  polymer-clay nano-composite sample [16]. Young's moduli of matrix and inclusion are taken as  $E_m = 3 \text{ GPa}$  and  $E_i = 300 \text{ GPa}$ , respectively. In this benchmark problem, one horizontal ( $\theta = 0$ )  $2 \mu\text{m}$  long inclusion with  $d_i = 5 \text{ nm}$  and aspect ratio equal to 400 is placed in the middle of the specimen. The matrix Poisson's ratio  $\nu_m$  is equal to 0.35.

For the reference numerical calculations, a  $600 \times 600$  uniform grid of bilinear quadrilateral elements is employed. The right-hand side edge is uniformly displaced by  $\delta = 0.05 \mu\text{m}$  (Fig. 3). Unlike similar studies [16,17], the inclusion is not perfectly bonded to the matrix and elastic sliding is therefore allowed (the interface tangential stiffness  $K_{bt}$  is set equal to  $0.025 \text{ N}/\mu\text{m}^3$ ).

*Analysis of the strain field in the matrix material.* While the displacement field in the matrix across the inclusion is continuous, some of the components of the strain field can be discontinuous.

The strain tensor components along the vertical lines shown in Fig. 4a are plotted in Fig. 4b-d. The vertical lines are aligned with the location of the integration points in the finite elements used to discretize the matrix material, thus allowing the direct sampling of the strain field. As shown in Fig. 4c, the shear component  $\varepsilon_{xy}$  of the matrix strain tensor is not continuous across the inclusion unlike the other two components  $\varepsilon_{xx}$  and  $\varepsilon_{yy}$  (Fig. 4b,d). These results have been confirmed with the double interface model presented in Ref. [33] which describes a fiber surrounded by the interface in a two-dimensional setting—this model is to be understood as the dimensional reduction of a solid fiber embedded in a three-dimensional body. As shown later, the classical ERS model [2] (Section 3.1.1) cannot reproduce this discontinuity in the gradient of the matrix displacement field.

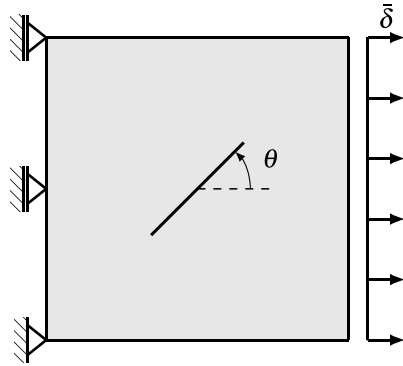


Fig. 3. Schematic of the benchmark problem with one inclusion.

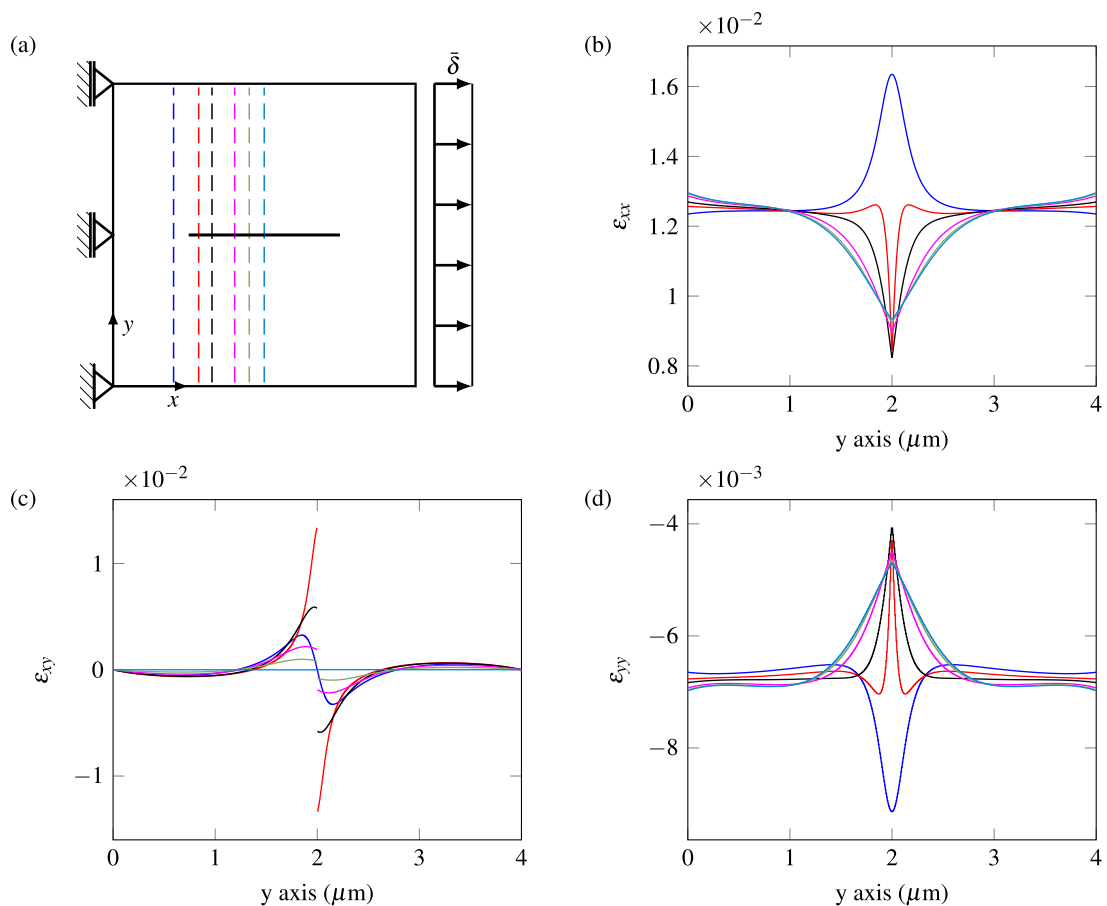


Fig. 4. (a) Schematic of the single inclusion problem with sampling lines for the strain tensor components reported in the other panels:  $\epsilon_{xx}$  (b),  $\epsilon_{xy}$  (c), and  $\epsilon_{yy}$  (d). The problem is solved using the conformal FEM model with a uniform  $600 \times 600$  Q4 discretization.

### 3. Mesh-independent models

In the reference model introduced in the previous section the inclusion was modeled using a conformal discretization. In principle, this is restrictive when handling a large number of inclusions. In this section, various numerical models that allow the inclusion to be positioned anywhere in the composite domain with respect to the underlying matrix discretization are discussed. At variance with the reference model, inclusion endpoints can be

placed within an element, and there is no theoretical limit on the number of inclusions that can be included in an element.

### 3.1. Embedded reinforcement models

Embedded reinforcement models cannot reproduce the discontinuity in the strain field discussed in the previous section. In these models, the displacement of an inclusion is usually determined indirectly, by means of the relative displacement  $\mathbf{u}_{rel}$  between inclusion and matrix which is taken as an additional field. This implies that the displacement field  $\mathbf{u}$  is decomposed into matrix component  $\mathbf{u}_m$ , valid in the matrix domain  $\Omega_m$ , and inclusion displacement component  $\mathbf{u}_d + \mathbf{u}_{rel}$ , valid in the inclusion domain  $\Omega_i$ , where the component  $\mathbf{u}_d$  is called concrete displacement [2] or duct displacement [27]; this quantity is later expressed as a function of the matrix displacement field  $\mathbf{u}_m$  of the elements crossed by the fiber. The matrix and inclusion stress tensors are defined as  $\boldsymbol{\sigma}_m$  and  $\boldsymbol{\sigma}_i$ , respectively. With this decomposition, the principle of virtual work, valid for many embedded reinforcement models [2,24,26,29], reads

$$\begin{cases} \int_{\Omega_m} \nabla^s \delta \mathbf{u}_m : \boldsymbol{\sigma}_m \, d\Omega_m + \int_{\Omega_i} \nabla^s \delta \mathbf{u}_d : \boldsymbol{\sigma}_i \, d\Omega_i = \int_{\Gamma_t} \delta \mathbf{u}_m \cdot \bar{\mathbf{t}} \, d\Gamma_t, \\ \int_{\Omega_i} \nabla^s \delta \mathbf{u}_{rel} : \boldsymbol{\sigma}_i \, d\Omega_i + \int_{\Gamma_{int}} \delta \mathbf{u}_{rel} \cdot \mathbf{t}_{int} \, d\Gamma_{int} = 0. \end{cases} \quad (7)$$

Note that there are only two independent fields in the above relations:  $\mathbf{u}_m$  and  $\mathbf{u}_{rel}$ .

As already mentioned in the introduction, with reference to high aspect ratio inclusions (Fig. 1a), the integrals over inclusion volume  $\Omega_i$  and inclusion–matrix interface  $\Gamma_{int}$  can be simplified to line integrals along the inclusion length  $l_i$ . With these modifications, and introducing Hooke’s law for matrix and inclusion constituents, the principle of virtual work (7) reads

$$\begin{cases} \int_{\Omega_m} \nabla^s \delta \mathbf{u}_m : \mathbf{D}_m : \nabla^s \mathbf{u}_m \, d\Omega_m + A_i \int_{l_i} \nabla^s \delta \mathbf{u}_d : (\mathbf{D}_i - \mathbf{D}_m) : \nabla^s \mathbf{u}_d \, dl_i + A_i \int_{l_i} \nabla^s \delta \mathbf{u}_d : \mathbf{D}_i : \nabla^s \mathbf{u}_{rel} \, dl_i \\ = \int_{\Gamma_t} \delta \mathbf{u}_m \cdot \bar{\mathbf{t}} \, d\Gamma_t, \\ A_i \int_{l_i} \nabla^s \delta \mathbf{u}_{rel} : \mathbf{D}_i : \nabla^s \mathbf{u}_d \, dl_i + A_i \int_{l_i} \nabla^s \delta \mathbf{u}_{rel} : \mathbf{D}_i : \nabla^s \mathbf{u}_{rel} \, dl_i + C_i \int_{l_i} \delta \mathbf{u}_{rel} \cdot (\bar{\mathbf{D}}_b \mathbf{u}_{rel}) \, dl_i = 0, \end{cases} \quad (8)$$

where  $\bar{\mathbf{D}}_b = \mathbf{R}^T \mathbf{D}_b \mathbf{R}$  is the rotated elastic interface tensor. The first integral is evaluated over the whole domain  $\Omega$  and, as a consequence, the effective stiffness  $\mathbf{D}_i - \mathbf{D}_m$  is introduced in the inclusion contribution (second integral) with  $\mathbf{D}_m$  and  $\mathbf{D}_i$  the matrix and inclusion isotropic elasticity tensors, respectively. This formulation is analogous to that by Radtke et al. [29] discussed in Section 3.1.5. The components  $\mathbf{u}_d$  and  $\mathbf{u}_{rel}$  of the inclusion displacement can be approximated in different manners as discussed next.

#### 3.1.1. Embedded reinforcement model with slip (ERS model)

In classical embedded reinforcement models with slip [2,24,26], slip DOFs are located along an inclusion axis (they are therefore defined in a coordinate system local to the inclusion) and at their intersections with matrix element edges. As it is assumed that an inclusion works mainly under axial deformation, the component of the displacement normal to the inclusion are neglected. Thus the inclusion displacement components  $\mathbf{u}_d$  and  $\mathbf{u}_{rel}$  in (8) are replaced by corresponding scalar quantities  $u_d$  and  $u_s$  in the direction of the inclusion axis leading to

$$\begin{cases} \int_{\Omega_m} \nabla^s \delta \mathbf{u}_m : \mathbf{D}_m : \nabla^s \mathbf{u}_m \, d\Omega_m + A_i (E_i - E_m) \int_{l_i} \delta u_{d,r} u_{d,r} \, dl_i + A_i E_i \int_{l_i} \delta u_{d,r} u_{s,r} \, dl_i = \int_{\Gamma_t} \delta \mathbf{u}_m \cdot \bar{\mathbf{t}} \, d\Gamma_t, \\ A_i E_i \int_{l_i} \delta u_{s,r} u_{d,r} \, dl_i + A_i E_i \int_{l_i} \delta u_{s,r} u_{s,r} \, dl_i + C_i \int_{l_i} \delta u_s K_{bt} u_s \, dl_i = 0, \end{cases} \quad (9)$$

where  $u_s$  is the slip of the inclusion, and the subscript  $r$  indicates a derivative with respect to the inclusion local axis.

### 3.1.2. $p$ -Enriched matrix embedded reinforcement model with slip ( $p$ ERS model)

In an attempt to improve the performance of the ERS model, an enriched finite element discretization is employed to approximate the matrix displacement field close to an inclusion. To this end, the high-order generalized finite element method (GFEM) approximation

$$\mathbf{u}_m(\mathbf{x}) = \sum_{\alpha=1}^n N_{m\alpha}(\mathbf{x}) \mathbf{u}_{m\alpha}^{\text{std}} + \sum_{\alpha=1}^n N_{m\alpha}(\mathbf{x}) \sum_{\beta=1}^{n_{\text{enr}}} \mathbf{u}_{m\alpha\beta}^{\text{enr}} P_{\beta\alpha}(\mathbf{x}) = \mathbf{N}_m \mathbf{d} \quad (10)$$

is adopted, where  $N_{m\alpha}$  are standard element nodal shape functions,  $n$  is the number of element nodes,  $n_{\text{enr}}$  is the number of enrichment terms,  $\mathbf{u}_{m\alpha}^{\text{std}}$  and  $\mathbf{u}_{m\alpha\beta}^{\text{enr}}$  are the standard and enrichment components of the matrix displacement vector, respectively, and  $\mathbf{N}_m$  and  $\mathbf{d}$  are the total (*i.e.*, including standard and enrichment terms) shape function matrix and displacement vector at the element level, respectively. The enrichment terms of the matrix displacement vector are defined following a hierarchical enrichment approach [34,35] using the generalized basis function vector

$$\{P_{\beta\alpha}\}_{\beta=1}^{n_{\text{enr}}} = \left\{ \frac{(x-x_\alpha)}{h_\alpha}, \frac{(y-y_\alpha)}{h_\alpha}, \frac{(x-x_\alpha)^2}{h_\alpha^2}, \frac{(x-x_\alpha)(y-y_\alpha)}{h_\alpha^2}, \frac{(y-y_\alpha)^2}{h_\alpha^2}, \dots \right\}. \quad (11)$$

In this study, and in the equation above, we have used up to 5 enrichment terms ( $n_{\text{enr}} = 5$ ) thus enriching the solution space with polynomials up to the second order. This enrichment leads to a quadratic approximation of the matrix displacement field with the first two terms ( $n_{\text{enr}} = 2$ ) and to a cubic approximation when all the terms ( $n_{\text{enr}} = 5$ ) are used. The scaling factor  $h_\alpha$  [35], usually taken as the diameter of the largest finite element sharing node  $\alpha$ , is here taken equal to unity for convenience. Since the hierarchical enrichment scheme is not stable for quadrilateral elements [36], a versatile technique based on the  $p$ -version of the finite element method [37] is employed to locally increase their approximation order in a similar manner as discussed in Section 5.2.

### 3.1.3. Discretization of the inclusion and displacement approximations

Inclusions are discretized into segments using the non-uniform sequence of points obtained from their intersection points with matrix element edges (if an inclusion ends within an element, the inclusion tip is taken as one of the inclusion segment endpoints). As defined earlier, the inclusion displacement is defined by  $u_d + u_s$ . We now discuss the approaches we follow to approximate both components.

*Inclusion displacement: Nonslip component.* With reference to an arbitrary inclusion segment with endpoints 1 and 2 (Fig. 1b), the nonslip component  $u_d$  of the inclusion displacement is written as

$$u_d = N_{i1} a_1 + N_{i2} a_2, \quad (12)$$

where  $a_1$  and  $a_2$  are the inclusion axial displacements at the two endpoints and  $N_{i1}(r)$  and  $N_{i2}(r)$  are linear Lagrange shape functions related to the segment endpoints and defined along the inclusion segment local axis.

Eq. (12) is expressed in terms of displacements in the global coordinate system as

$$u_d = [N_{i1} \cos \theta_x \quad N_{i1} \cos \theta_y \quad N_{i2} \cos \theta_x \quad N_{i2} \cos \theta_y] \mathbf{a}_d, \quad (13)$$

where  $\theta_x$  and  $\theta_y$  are the directional angles defined in the global  $xy$  coordinate system (Fig. 1b), and the displacement vector

$$\mathbf{a}_d = [a_{x1} \quad a_{y1} \quad a_{x2} \quad a_{y2}]^T \quad (14)$$

is obtained from the interpolation of the nodal displacement vector at the elemental level (matrix element) to endpoints  $(x_1, y_1)$  and  $(x_2, y_2)$  of the inclusion element related to that matrix element (*i.e.*, using the approximation (10) evaluated at the inclusion endpoints).

The displacement  $u_d$  and its derivative are therefore

$$u_d = \mathbf{N}_d \mathbf{H} \mathbf{d} \quad \text{and} \quad u_{d,r} = \mathbf{B}_d \mathbf{H} \mathbf{d}, \quad (15)$$

with

$$\mathbf{N}_d = [N_{i1} \cos \theta_x \quad N_{i1} \cos \theta_y \quad N_{i2} \cos \theta_x \quad N_{i2} \cos \theta_y] \quad (16)$$

and

$$\mathbf{B}_d = [N_{i1,r} \cos \theta_x \quad N_{i1,r} \cos \theta_y \quad N_{i2,r} \cos \theta_x \quad N_{i2,r} \cos \theta_y], \quad (17)$$

where the transformation matrix

$$\mathbf{H} = [\mathbf{H}^{\text{std}} \quad \mathbf{H}_{\beta=1}^{\text{enr}} \quad \dots \quad \mathbf{H}_{\beta=n_{\text{enr}}}^{\text{enr}}], \tag{18}$$

with standard component

$$\mathbf{H}^{\text{std}} = \begin{bmatrix} N_{m1}|_1 & 0 & \dots & N_{mn}|_1 & 0 \\ 0 & N_{m1}|_1 & \dots & 0 & N_{mn}|_1 \\ N_{m1}|_2 & 0 & \dots & N_{mn}|_2 & 0 \\ 0 & N_{m1}|_2 & \dots & 0 & N_{mn}|_2 \end{bmatrix} \tag{19}$$

and enrichment component

$$\mathbf{H}_{\beta}^{\text{enr}} = \begin{bmatrix} P_{\beta,1}N_{m1}|_1 & 0 & \dots & P_{\beta,n}N_{mn}|_1 & 0 \\ 0 & P_{\beta,1}N_{m1}|_1 & \dots & 0 & P_{\beta,n}N_{mn}|_1 \\ P_{\beta,1}N_{m1}|_2 & 0 & \dots & P_{\beta,n}N_{mn}|_2 & 0 \\ 0 & P_{\beta,1}N_{m1}|_2 & \dots & 0 & P_{\beta,n}N_{mn}|_2 \end{bmatrix}, \tag{20}$$

links  $\mathbf{a}_d$  to the matrix nodal displacements vector  $\mathbf{d}$  at the element level. In these expressions, the matrix shape functions are evaluated at the discontinuity segment endpoints. The above derivations therefore show that the  $u_d$  component of the inclusion displacement is computed using information from the matrix displacement field.

*Inclusion displacement: Slip component.* The displacement slip component  $u_s$  and its derivative can be approximated as

$$u_s = \mathbf{N}_s \mathbf{b}_s \quad \text{and} \quad u_{s,r} = \mathbf{B}_s \mathbf{b}_s, \tag{21}$$

where  $\mathbf{b}_s = [b_1, b_2]^T$  is the vector of endpoint slip DOFs, and

$$\mathbf{N}_s = [N_{i1} \quad N_{i2}] \quad \text{and} \quad \mathbf{B}_s = [N_{i1,r} \quad N_{i2,r}]. \tag{22}$$

### 3.1.4. Discretized system of equations

Introducing the discretized expressions (10), (15) and (21) into the principle of virtual work (9) yields the system of equations

$$\begin{bmatrix} \mathbf{K}_{mm} & \mathbf{K}_{mi} \\ \mathbf{K}_{im} & \mathbf{K}_{ii} \end{bmatrix} \begin{bmatrix} \mathbf{d} \\ \mathbf{b} \end{bmatrix} = \begin{bmatrix} \mathbf{f}_m \\ \mathbf{0} \end{bmatrix} \tag{23}$$

valid at the element level for the case of a single inclusion. The vectors  $\mathbf{d}$  and  $\mathbf{b}$  contain matrix and slip DOFs, respectively,  $\mathbf{f}_m$  is the external force vector, and the stiffness matrix submatrices are

$$\begin{aligned} \mathbf{K}_{mm} &= \int_{\Omega_e} \mathbf{B}_m^T \mathbf{D}_m \mathbf{B}_m \, d\Omega_e + A_i \int_L \mathbf{H}^T \mathbf{B}_d^T \bar{E} \mathbf{B}_d \mathbf{H} \, dr, \\ \mathbf{K}_{mi} &= A_i \int_L \mathbf{H}^T \mathbf{B}_d^T E_i \mathbf{B}_s \, dr, \\ \mathbf{K}_{im} &= A_i \int_L \mathbf{B}_s^T E_i \mathbf{B}_d \mathbf{H} \, dr, \\ \mathbf{K}_{ii} &= A_i \int_L \mathbf{B}_s^T E_i \mathbf{B}_s \, dr + C_i \int_L \mathbf{N}_s^T K_{bt} \mathbf{N}_s \, dr, \end{aligned} \tag{24}$$

where  $\Omega_e$  is the domain of the element and  $L$  is the length of the inclusion segments within it. This discretized system of equation is valid for the ERS and  $p$ ERS models. For cases with more than one inclusion, the system of equations is modified as shown in [27] or [29].

### 3.1.5. Slip enriched partition of unity model (slipPoU)

Radtke et al. [29] proposed an approach alternative to the ERS model. In their formulation, in which the displacement field is decomposed as in Section 3.1, the partition of unity property of finite element shape functions is employed to enrich the matrix displacement field with information about the inclusion kinematics. Matrix-inclusion relative displacement DOFs expressed in the global coordinate system are assigned to all the nodes of elements intersected by an inclusion. Following the procedure described in [29] yields a global system of equations that can be written as (23) with submatrices

$$\begin{aligned} \mathbf{K}_{mm} &= \int_{\Omega_e} \mathbf{B}_m^T \mathbf{D}_m \mathbf{B}_m \, d\Omega_e + A_i \int_L \mathbf{B}_m^T (\mathbf{D}_i - \mathbf{D}_m) \mathbf{B}_b \, dr, \\ \mathbf{K}_{mi} &= A_i \int_L \mathbf{B}_m^T \mathbf{D}_i \mathbf{B}_b \, dr, \\ \mathbf{K}_{im} &= A_i \int_L \mathbf{B}_m^T \mathbf{D}_i \mathbf{B}_b \mathbf{H} \, dr, \\ \mathbf{K}_{ii} &= A_i \int_L \mathbf{B}_m^T \mathbf{D}_i \mathbf{B}_b \, dr + C_i \int_L \mathbf{N}_b^T \bar{\mathbf{D}}_b \mathbf{N}_b \, dr, \end{aligned} \quad (25)$$

where  $\mathbf{N}_m$  and  $\mathbf{B}_b = \mathbf{B}_m$  are the standard FEM shape function and derivative matrices, respectively. In this model, the number of DOFs in an element intersected by an inclusion doubles to take into account the additional relative displacement DOFs defined at each node, thus yielding a larger system of equations compared to that obtained with the ERS model described in the previous section. The relative displacement is approximated by making reference to the shape functions of the parent element. In the applications discussed later in this paper, the results of this model are provided only for the sake of comparison with the more efficient ERS model. As discussed in Section 2.1, we do not allow the relative displacement in the normal direction by choosing large values of the interface normal stiffness  $K_{bn}$ .

### 3.2. Strain discontinuity enriched embedded reinforcement model with slip (sdERS model)

A simple approach to allow a strain discontinuity in an embedded formulation is to enrich the displacement approximation of the matrix material with a weak discontinuity enrichment function using the partition of unity enrichment method [18,34,38,39]. This approach is applied to the embedded reinforcement model proposed by Goudarzi and Simone [33]. The governing equations for the inclusion depicted in Fig. 2b can be obtained by a modification of the equations derived for the conformal model in Fig. 2a. The goal of this modification is to design a kinematic field in which the displacement is continuous and its gradient can be discontinuous, similar to the strain fields obtained with the conformal model described in Section 2.1. This can be achieved by adopting the enriched approximation

$$\mathbf{u}_m(\mathbf{x}) = \sum_{\alpha=1}^n N_{m\alpha}(\mathbf{x}) \mathbf{u}_{m\alpha}^{\text{std}} + \sum_{\alpha=1}^n N_{m\alpha}(\mathbf{x}) \mathcal{Y}(\mathbf{x}) \mathbf{u}_{m\alpha}^{\text{enr}} \quad (26)$$

for the matrix displacement field expressed at the elemental level in the global coordinate system, where  $\mathbf{u}_{m\alpha}^{\text{std}}$  and  $\mathbf{u}_{m\alpha}^{\text{enr}}$  are the standard and enrichment matrix displacement vectors, respectively. To ensure continuous displacements with discontinuous gradients, the enrichment function [19]

$$\mathcal{Y}(\mathbf{x}) = \sum_{\alpha=1}^n N_{m\alpha}(\mathbf{x}) |\zeta_\alpha| - \left| \sum_{\alpha=1}^n N_{m\alpha}(\mathbf{x}) \zeta_\alpha \right| \quad (27)$$

is employed, where  $\zeta_\alpha$  is the level-set function that measures the shortest distance between an element node and the inclusion. This enrichment function ensures that the displacement approximation can reproduce the strain fields in Fig. 4. The displacement vector  $\mathbf{d}_{\text{int}}$  in (3) and the interface shape function matrix  $\mathbf{N}_{\text{int}}$  in (4) are modified accordingly as

$$\mathbf{d}_{\text{int}} = [\mathbf{u}_{i1} \quad \mathbf{u}_{i2} \quad | \quad \mathbf{u}_{m1}^{\text{std}} \quad \cdots \quad \mathbf{u}_{mn}^{\text{std}} \quad | \quad \mathbf{u}_{m1}^{\text{enr}} \quad \cdots \quad \mathbf{u}_{mn}^{\text{enr}}]^T \quad (28)$$

and

$$\mathbf{N}_{\text{int}} = [N_{i1} \mathbf{I} \quad N_{i2} \mathbf{I} \quad | \quad -N_{m1} \mathbf{I} \quad \cdots \quad -N_{mn} \mathbf{I} \quad | \quad -\mathcal{Y} N_{m1} \mathbf{I} \quad \cdots \quad -\mathcal{Y} N_{mn} \mathbf{I}], \quad (29)$$

respectively, where  $\mathbf{I}$  is the  $2 \times 2$  identity matrix and the other quantities have been defined earlier. For the discretization of the inclusion we make reference to Section 2.1.

#### 4. Comparative analysis of the performance of embedded reinforcement models

As mentioned in Section 2.2, a discontinuity in the matrix strain field is expected across embedded inclusions. The discrete models described in Section 3.1 do not capture intra-element discontinuities. Those simplified models are however significantly cheaper when dealing with large inclusion volumes compared with the conformal or discontinuous approaches described in Sections 2.1 and 3.2, respectively. The approximation features of these discrete models is assessed by repeating the analysis of the strain field in Section 2.2; a further assessment is performed by means of convergence studies on one or multiple inclusion composites. Reference is made to the material parameters and geometrical properties of the polymer/clay nanocomposite discussed in Section 2.2.

##### 4.1. Single inclusion

The case of a single inclusion is considered first. A detailed study of the strain components and a mesh convergence study are provided.

##### 4.1.1. Strain distribution across the inclusion

The study presented in Section 2.2 is repeated here by comparing strain fields obtained with conformal FEM model (Section 2.1), ERS model (Section 3.1.1), and strain discontinuity enriched ERS (sdERS) model (Section 3.2). The FEM reference solution (thin cyan line) is obtained with a uniform  $600 \times 600$  Q4 conformal discretization, while a uniform  $100 \times 100$  (Q4) mesh is used for both ERS models. Strains are sampled at integration point locations along a vertical line located near the tip of the inclusion (Fig. 5a). The most evident difference in the results obtained with the two ERS models lies in the continuity of the mixed component of the strain tensor ( $\varepsilon_{xy}$ ), with the ERS model (red line) being clearly unable to represent the discontinuity reported by the reference conformal FEM model (Fig. 5c). Other notable difference is the overall resemblance of the solutions obtained with the enriched model (blue line) and the reference FEM solution around the inclusion (see insets in Fig. 5b,d), where the ERS model shows a piecewise constant strain profile. Differences are however minute far from the inclusion.

##### 4.1.2. Convergence study

To assess the quality of the strain discontinuity enriched ERS model (Section 3.2), a mesh convergence study is performed. The role of the bond stiffness is evaluated by adopting three different tangential stiffness values  $K_{bt}$  (0.025, 0.05, and 0.25  $\text{N}/\mu\text{m}^3$ ). Fig. 6 shows the resulting slip profiles obtained with a conformal FEM analysis using a  $600 \times 600$  uniform grid of bilinear quadrilateral elements.

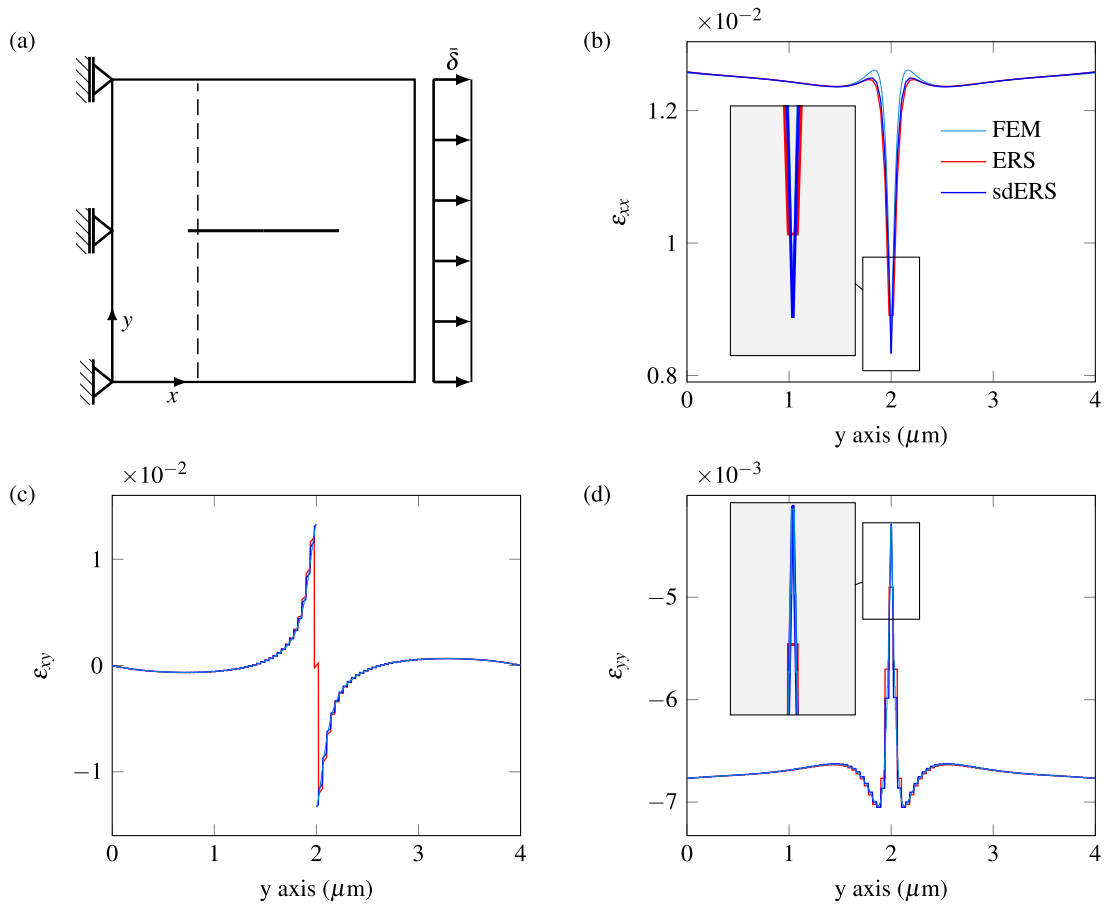
As a closed-form analytical solution is not available for this problem, the reference strain energy values used in the convergence study are estimated. Following [40], an estimate of the exact strain energy is extracted using hierarchical sequences of finite element spaces by means of the expression

$$\frac{\pi_3 - \pi}{\pi_2 - \pi} = \left( \frac{\pi_2 - \pi}{\pi_1 - \pi} \right)^Q \quad \text{with} \quad Q = \log \frac{N_2}{N_3} \left( \log \frac{N_1}{N_2} \right)^{-1}, \quad (30)$$

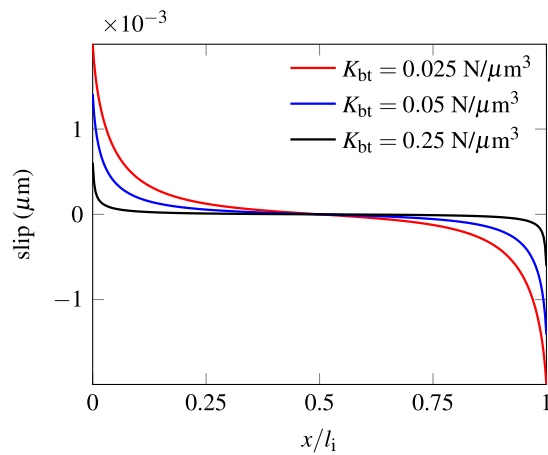
with  $N_1 < N_2 < N_3$  the numbers of degrees of freedom and  $\pi_1$ ,  $\pi_2$ , and  $\pi_3$  the corresponding strain energy values. For the numerical solutions, uniformly refined unstructured T3 meshes with 9013, 34,901 and 138,571 nodes are employed. Eq. (30) is then solved for the estimated exact strain energy  $\pi$  that is used as the reference value in the mesh convergence study.

Fig. 7 compares the results obtained with the strain discontinuity enriched ERS (sdERS) model against those obtained with the ERS model (Section 3.1.1) with T3 and Q4 discretizations, the  $p$ -enriched matrix ERS ( $p$ ERS) model (Section 3.1.2) with local quadratic ( $n_{\text{enr}} = 2$ ) and cubic ( $n_{\text{enr}} = 5$ ) approximations, and the slip enriched partition of unity (slipPoU) model (Section 3.1.5) for three values of the bond stiffness.

The performance of the ERS model with both discretizations and that of the slipPoU model are indistinguishable. Expectedly, the strain discontinuity enriched ERS model performs better compared to the ERS model. This is attributed to the appropriate representation of the strain field in elements crossed by the inclusion. As discussed earlier, the ERS model cannot represent discontinuities in the strain field across an inclusion. To improve the quality



**Fig. 5.** (a) Schematic of the single inclusion problem with sampling line for the strain tensor components reported in the other panels:  $\epsilon_{xx}$  (b),  $\epsilon_{xy}$  (c), and  $\epsilon_{yy}$  (d). The problem is solved using the conformal FEM, ERS, and strain discontinuity enriched ERS (sdERS) models with a uniform  $100 \times 100$  Q4 discretization. (For interpretation of the references to color in this figure legend, the reader is referred to the web version of this article.)



**Fig. 6.** Slip profiles corresponding to various interface tangential stiffness values adopted in the mesh convergence study (Section 4.1.2).

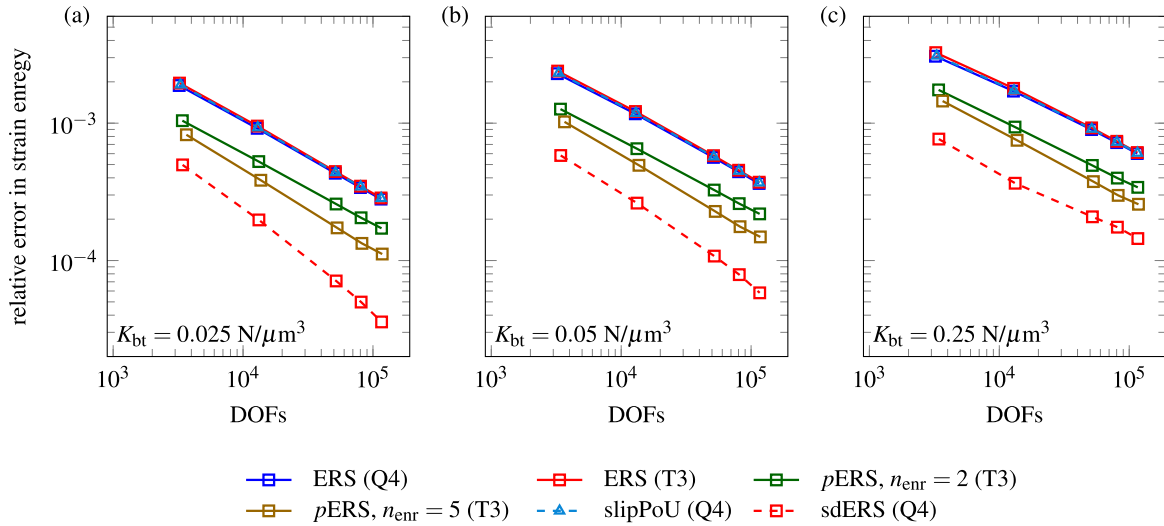


**Fig. 7.** Relative errors in strain energy for the single inclusion problem under uniform mesh refinements. Results are shown for the ERS model with T3 and Q4 discretizations, the  $p$ -enriched matrix ERS ( $p$ ERS) model with local quadratic ( $n_{\text{enr}} = 2, p = 2$ ) and cubic ( $n_{\text{enr}} = 5, p = 3$ ) approximations, the slip enriched partition of unity (slipPoU) model, and the strain discontinuity enriched ERS (sdERS) model for three values of the bond stiffness.

of the solution, the displacement field in the elements crossed by an inclusion is therefore enhanced by elevating its approximation order. The results show the improved performance of the  $p$ ERS model compared to that of the ERS. Although the strain discontinuity enriched ERS model provides the most accurate solution, it can considerably increase the complexity of the numerical implementation. Indeed, this model requires the integration of the weak enrichment function (27) using integration subdomains, and this task can be prohibitively expensive when dealing with dense inclusion distributions. A simpler strategy, although less effective, is to use high order displacement approximations ( $p$ ERS).

#### 4.2. Randomly dispersed inclusions

The goal of this section is to show the effectiveness of the models described in the previous section in the analysis of a composite with a relative large number of interacting inclusions. This is a situation in which ERS models are key to this type of numerical exercise as conformal FEM and strain discontinuity enriched ERS models are very expensive options.

Fig. 8 shows a typical periodic square unit cell setup used in this mesh convergence study with 367 randomly dispersed and non-intersecting clay platelets with a spatial arrangement similar to that reported in Ref. [17]. The periodic boundary conditions described in Ref. [41] are imposed on the unit cell, with the horizontal displacement  $\delta$  set equal to  $0.05 \mu\text{m}$  at the lower right-hand side node (Fig. 8). As in the previous case, the inclusions are not perfectly bonded and the elastic interface tangent  $K_{\text{bt}}$  is set equal to  $0.05 \text{ N}/\mu\text{m}^3$ . The inclusions have all the same length  $l_i = 0.52 \mu\text{m}$ . The approximated reference strain energy is extracted with the procedure described earlier for the single inclusion case using the ERS model (Section 3.1.1) with the matrix discretized using uniform grids of  $250 \times 250, 500 \times 500$  and  $1000 \times 1000$  bilinear quadrilateral elements.

Fig. 9 shows the results obtained with the finest ERS discretization for the distribution in Fig. 8 in terms of the von Mises stress field together with axial stress and slip fields for three inclusions. These results indicate that solution fields local to an inclusion vary depending on its position in the composite, an information that mean-field approaches cannot predict.

##### 4.2.1. Mesh convergence study with uniform mesh refinement

Fig. 10a shows the relative error plots for the strain energy obtained with the ERS model (Section 3.1.1) and the slip enriched partition of unity (slipPoU) model (Section 3.1.5). The domain is discretized using bilinear

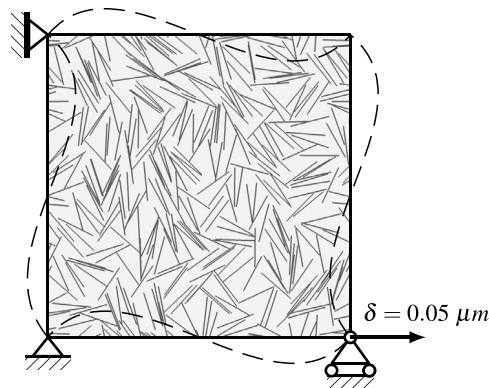


Fig. 8. Periodic random distribution of 367 non-intersecting inclusions used in the multiple inclusion problem.

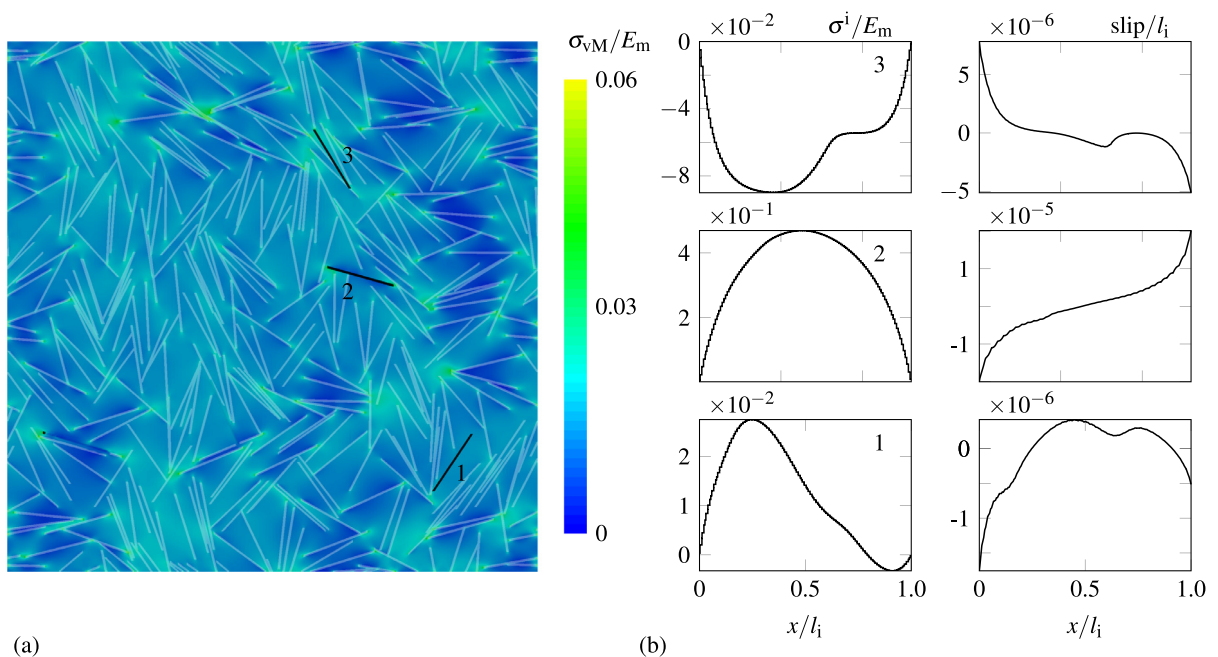
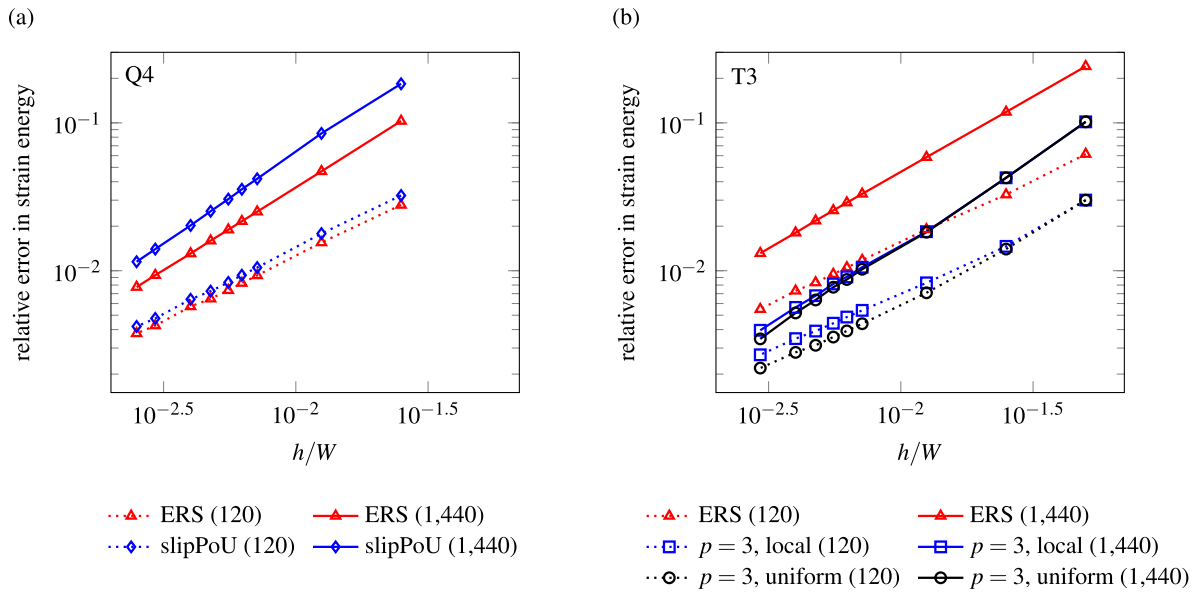


Fig. 9. (a) von Mises stress distribution for the problem with 367 randomly-distributed inclusions. (b) Axial stress and slip fields for the three labeled inclusions in panel (a).

quadrilateral elements uniformly refined. Both models rely on similar assumptions, the major difference being the allocation of slip DOFs—slip DOFs are assigned to all the nodes of a crossed element in the slipPoU model, while in the ERS model they are only assigned to the intersection points between inclusion and element edges and are aligned along the inclusion axis. Unlike the case of the single inclusion problem discussed in the previous section (Fig. 7), the curves for a given number of inclusions do not overlap and the error produced by the slipPoU model is larger.

The same study is now repeated using the  $p$ -enriched matrix ERS ( $p$ ERS) model proposed in Section 3.1.2 with a T3 discretization generated by splitting each quadrangular element in a regular structured grid into two triangles. Linear ( $n_{\text{enr}} = 0$ , equivalent to ERS) and cubic ( $n_{\text{enr}} = 5$ ) approximations are considered. This enrichment strategy is advantageous over traditional Lagrange cubic elements because it can be applied locally to certain element groups (those crossed by the inclusions), while keeping the order of the approximation unchanged in the rest of domain (we refer to this enrichment scheme as local). For a fair comparison, the same approximation is also employed throughout the whole domain (global enrichment scheme). Fig. 10b shows the error plots for different cases. Using



**Fig. 10.** Plots of the relative error in strain energy for the problem with the randomly-distributed inclusions for two inclusion distributions (number of inclusions shown between parentheses). Results are shown for (a) the ERS model and the slip enriched partition of unity (slipPoU) model using uniform Q4 discretizations, (b) the ERS model and the  $p$ -enriched matrix ERS ( $p$ ERS) model with cubic ( $n_{\text{enr}} = 5$ ,  $p = 3$ ) approximation for all elements (uniform) or for elements intersected by the inclusions (local) using uniform T3 discretizations. Element and domain size are  $h$  and  $W = 4 \mu\text{m}$ , respectively.

a cubic approximation leads in any case to lower errors compared to the results obtained with the ERS model. The use of a global enrichment strategy does not seem to be advantageous as the error is close to that obtained with the local enrichment. Although the rate of convergence is improved for  $p$ ERS compared to ERS, the improvements are not significant due to artificial continuity of the strain fields.

#### 4.2.2. Mesh convergence study with adaptive refinement

The uniform refinement case just discussed is not efficient as it leads to the refinement of regions where steep gradients are absent. Also, close to the elements crossed by an inclusion, inaccurate intra-element strains are present and a finer discretization would be preferred. To address these problems, we employ an adaptive refinement procedure based on a strain energy error estimator. For the local mesh refinement in regions with high stress concentration, the technique of Zienkiewicz and Zhu [42] is used. Reference (enhanced) strain fields are predicted using the super-convergent patch recovery technique [43]. For the local refinement of triangular element meshes we use the longest edge bisection algorithm by Rivara [44], while for quadrilateral meshes we use a non-conformal adaptive mesh refinement technique with hanging nodes. A hanging node is treated by constraining it to surrounding matrix element nodes, with the multifreedom constraint relations satisfied by the use of the master–slave elimination technique.

Strain energy convergence plots are shown in Fig. 11 for quadrilateral and triangular element discretizations and for different numbers of inclusions. Compared with the uniform refinement,  $h$ -adaptivity reduces the computational costs in all cases by eliminating unnecessary mesh refinement. Additionally, as shown in Fig. 11b, if  $h$ -adaptivity is combined with a local high order enrichment scheme ( $p$ ERS) applied only in elements crossed by an inclusion, the numerical performance is enhanced and errors are considerably reduced.

Fig. 12 shows typical discretizations obtained with the adaptive refinement scheme for the case with 367 inclusions. Note how the adaptive refinement algorithm identified the regions around the inclusion where mesh refinement is most needed—compare the different discretizations around inclusions 1 and 2 (labeled in Fig. 9) with the corresponding stress field.

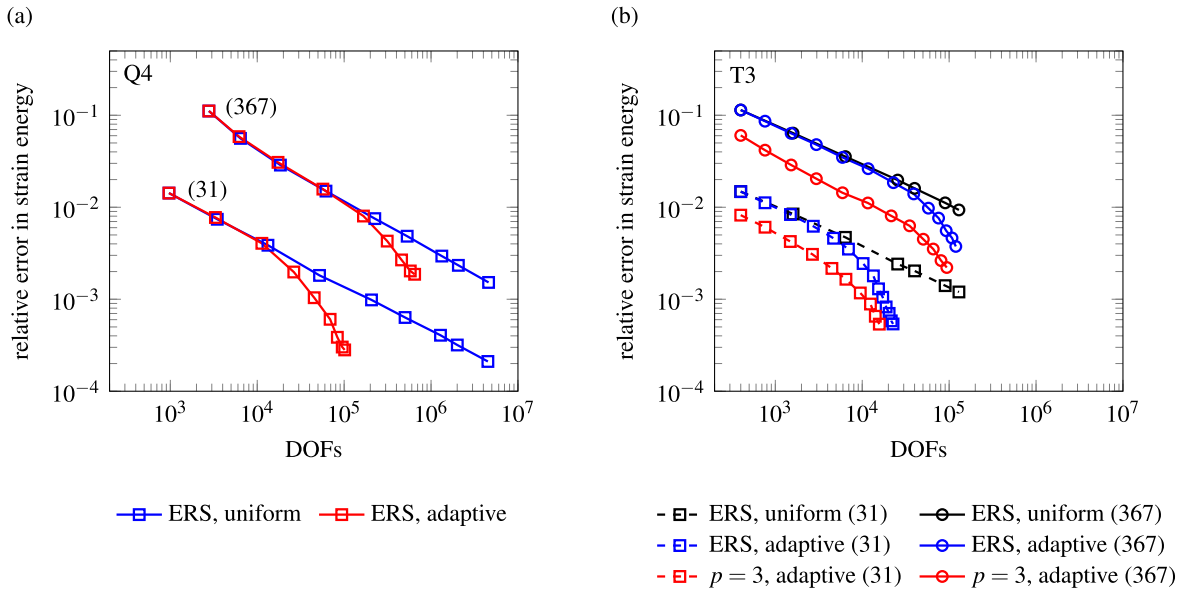


**Fig. 11.** Relative error in strain energy for the problem with the randomly-distributed inclusions for two inclusion distributions (number of inclusions shown between parentheses). Results are shown for (a) the ERS model with uniform and adaptive Q4 discretizations, and (b) the ERS model and the  $p$ -enriched matrix ERS ( $p$ ERS) model with cubic ( $n_{\text{enr}} = 5$ ,  $p = 3$ ) approximation for elements intersected by the inclusions using uniform and adaptive T3 discretizations.

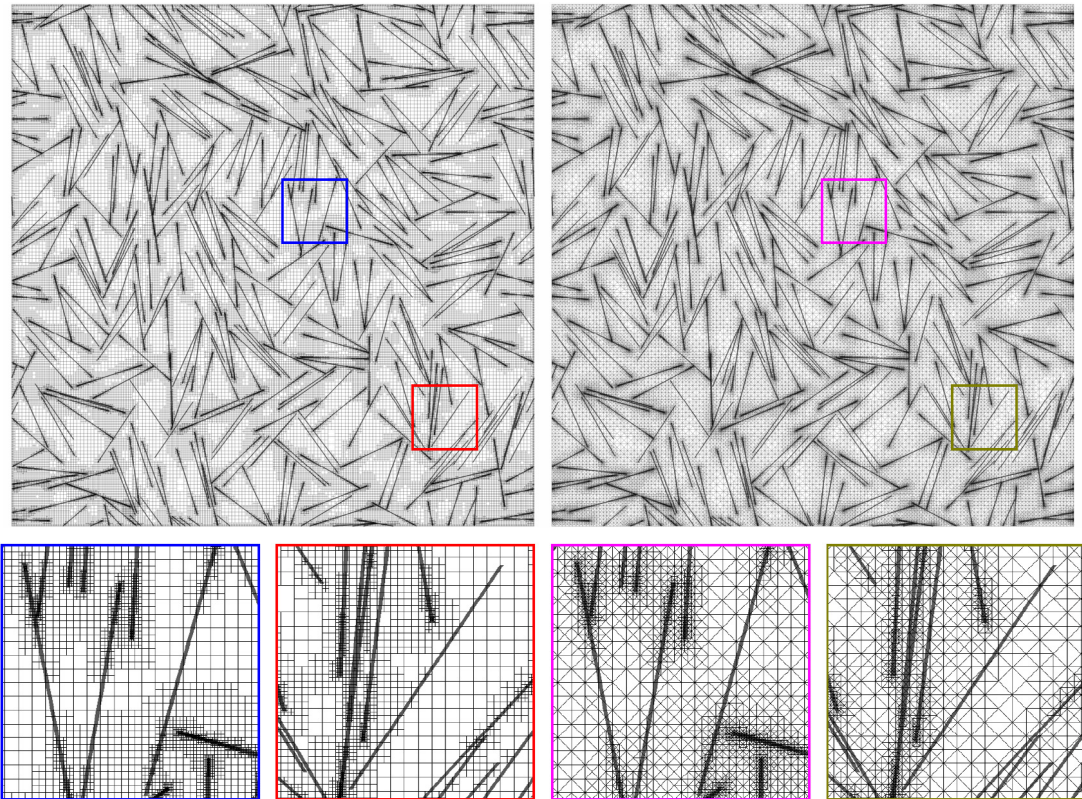


**Fig. 12.** Adaptively refined meshes using Q4 and T3 discretizations for the case with 367 randomly distributed inclusions.

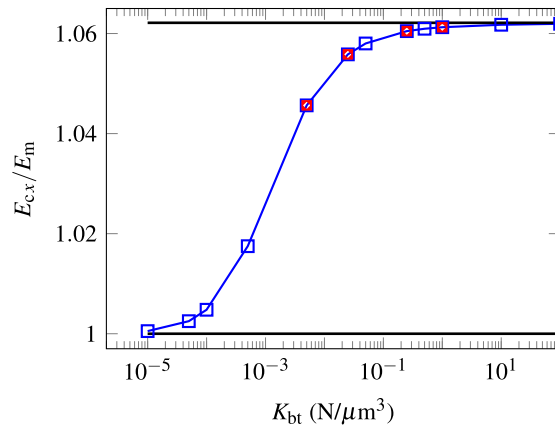


**Fig. 13.** A situation of near perfect bonding between matrix and inclusion can be achieved by increasing the interface tangential bond stiffness value. The normalized effective elastic Young's modulus of the composite with 21 aligned inclusions is plotted as a function of the interface tangential stiffness. (For interpretation of the references to color in this figure legend, the reader is referred to the web version of this article.)

## 5. Slip profiles

So far the embedded techniques were assessed in terms of their global response. In this section we demonstrate that the slip is, under certain conditions, not smooth due to the presence of unphysical oscillations and provide some remedies to reduce them. In all the simulations performed with an embedded reinforcement approach, each inclusion segment contained in a matrix element has been uniformly refined in eight segments. A Newton-Cotes integration scheme is used, and the reported slip values are sampled at the integration point locations (and these coincide with the inclusion elements nodes in each matrix element). As the inclusion segments are sufficiently refined, the slip profiles do not noticeably change by including more sampling points along each inclusion segment.

### 5.1. Slip oscillations

The problem of the oscillations in the slip profile is illustrated with reference to the two-dimensional one-inclusion composite depicted in Fig. 3 with  $\theta = 0.7$  rad with input parameters and boundary conditions described in Section 2.2.

Before performing slip tests on the single inclusion problem, the effect of the interface stiffness  $K_{bt}$  on the homogenized Young's modulus  $E_{cx}$  of the composite is studied in Fig. 13; for a sensible increase of  $E_{cx}$ , 21 aligned inclusions are considered. The profile of the homogenized Young's modulus plateaus for  $K_{bt} > 10 N/\mu m^3$ . This means that for those values of the bond stiffness, the inclusion can be regarded as perfectly bonded to the matrix with negligible slip; for all other values of the bond stiffness, the slip is physically meaningful.

With reference to the single inclusion problem, Fig. 14 shows the slip profiles obtained for the bond stiffness values marked by the red squares in Fig. 13. The profiles are extracted from solutions obtained with relatively coarse and fine discretizations with bilinear quadrilateral elements and are accompanied by predictions obtained with a conformal  $600 \times 600$  uniform grid of bilinear quadrilateral elements. The results indicate that oscillations in the slip profile emerge for relatively large values of the bond stiffness, while the reference conformal FEM predictions remain smooth for the whole range of interface stiffness values.

The results in this subsection are obtained with the embedded reinforcement model proposed in Ref. [33], which is endowed with inclusion displacement DOFs. Results not reported here indicate that the inclusion displacement is a smooth function, irrespective of material parameters and underlying mesh quality, therefore implying that the non-smoothness of the slip profile is due to the non-smoothness of the interpolated matrix displacement field at the inclusion nodes. Identical oscillatory results, not reported here, are also obtained with all the embedded reinforcement models discussed in Section 3.1, which are endowed with slip DOFs—some mild

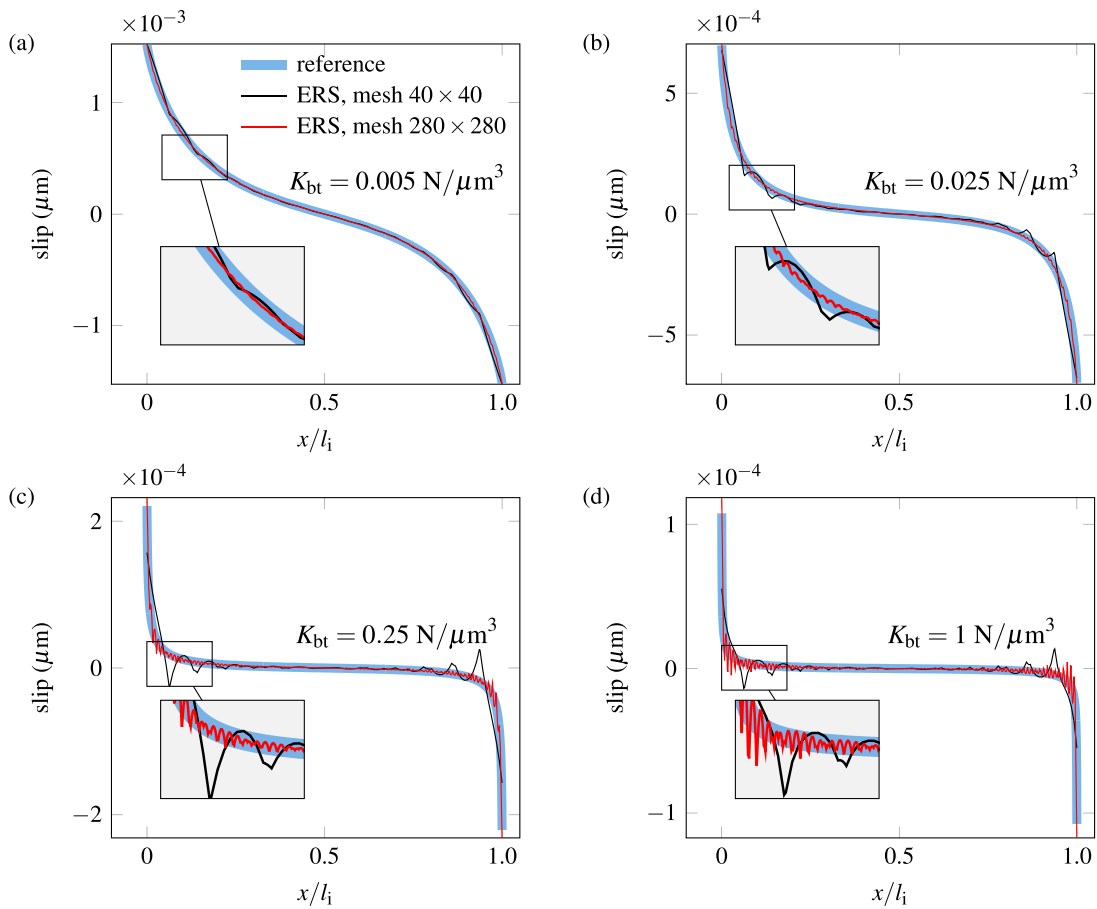


**Fig. 14.** Slip profiles for the single inclusion problem obtained with the ERS model corresponding to the bond stiffness values marked by the red squares in Fig. 13. The results are shown for relatively coarse and fine Q4 discretizations and are accompanied by the reference slip profiles obtained with a conformal FEM approach (uniform  $600 \times 600$  Q4 discretization).

oscillations are indeed present in the results discussed earlier in the paper (slip profile of the second inclusion in Fig. 9b). Both models share the inability to reproduce a discontinuity in the matrix strain field across an inclusion, thus suggesting that slip oscillations are related to the matrix strain field. As discussed earlier in Section 3.2 enriching the matrix displacement field with a weak discontinuity function endows the model with a discontinuous strain field across an inclusion (its effectiveness in addressing this problem is discussed next). The strain discontinuity enriched ERS model is however expensive, and in the next section we explore the effectiveness of alternative solutions using the models described in Section 3.1. As a side note, oscillations in the slip profile were observed using either Gauss or Newton-Cotes quadrature schemes and therefore are not of the type discussed in Ref. [45].

Although the results in this section are specific to an example and a set of material parameters, results not reported here indicate that similar oscillatory results are obtained with very different material properties. Our numerical evidence seems to imply that oscillations are an intrinsic feature of these models, rather than a feature triggered by a special combination of material parameters. As of now, we can only suggest to produce a study similar to that in Fig. 13 and verify the existence of oscillatory slip profiles if the chosen value of the bond stiffness is close to that considered as the perfect bond threshold. Needless to say an erroneous prediction of the slip profile might have adverse consequences in the interpretation of the results or in nonlinear analyses as nonlinearity might be artificially triggered.

## 5.2. Approaches to improve the slip profiles

As the quality of the matrix displacement field in elements crossed by an inclusion seems to dictate the quality of the slip profile along that inclusion, the strategies discussed next rely on improvements of the approximation of the matrix displacement field when needed. An optimal solution requires the development of intra-element discontinuous displacement gradients in elements crossed by inclusions. Such weak displacement discontinuity can be reproduced with the strain discontinuity enriched ERS model proposed in Section 3.2. An alternative approach consists in the approximation of the discontinuity in the strain field by means of more sophisticated displacement approximations that do not introduce a weak discontinuity enrichment in the displacement field but have the necessary flexibility to represent it in an appropriate manner. To obtain a model with such capabilities, we have considered the embedded reinforcement model proposed in Ref. [33] and replaced its shape functions with moving least squares (MLS) [46,47] functions over the entire domain (this is an element free discretization for the matrix domain similar to that proposed by Nayroles et al. [48]). With reference to the sdERS model in Section 3.2, the enrichment component in (26) is removed and the matrix shape functions are replaced with MLS shape functions constructed using a linear basis. A regular cubic spline weight function is used [49], while the size of support domain is set equal to three times the nodal spacing to ensure a smooth stress profile.

We also tested our hypothesis on the quality of the displacement field in the matrix by employing a model based on the  $p$ -version of the finite element method ( $p$ -FEM) [37,50]. This model, conceptually similar to the  $p$ -enriched matrix ERS model presented in Section 3.1.2, employs hierarchical Legendre polynomials and arbitrary selective order elevation (up to order 7 in this study) in elements crossed by an inclusion. Its implementation is similar to that described for the MLS shape functions.

As a measure of the quality of the improved approximations, we perform a convergence study on the slip profile by measuring the absolute error through its  $L_2$  norm defined as

$$\|e_s\| = \frac{\sqrt{\int_{l_i} \|s_{\text{ref}} - s_h\|^2 dr}}{\sqrt{\int_{l_i} \|s_{\text{ref}}\|^2 dr}}, \quad (31)$$

where  $s_h$  and  $s_{\text{ref}}$  are the approximated and reference slip values, respectively. The integrals are evaluated along the inclusion axis,  $l_i$ , and the reference slip solution  $s_{\text{ref}}$  is extracted from a reference FEM solution (Section 2.2) obtained with a  $600 \times 600$  uniform grid of bilinear quadrilateral elements.

The results of this study are reported in Fig. 15 in terms of the error convergence plots for three different  $K_{\text{bt}}$  values, and in Figs. 16 and 17 in terms of the slip profiles for the two largest  $K_{\text{bt}}$  values. An improved approximation of the displacement field in the matrix material has a positive impact on the solution. In terms of local quantities, a visual inspection of the slip profiles clearly shows that compared to a basic ERS formulation all proposed approaches reduce the oscillations in the slip profiles, with the  $p$ -FEM based approximation performing better. The least improvement seems to be related to the strain discontinuity enriched ERS model. The results in terms of a global measure however (Fig. 15) indicate that the MLS based model performs the worse. Noteworthy, the  $p$ -FEM based approximation performs better than the strain discontinuity enriched ERS model only for  $p \geq 4$ .

Although slip oscillations are attributed to the poor quality of intra-element displacements related to the artificial continuity of the strain field in the ERS model, oscillations are still present in the sdERS model where the strain discontinuity is explicitly described. At present we cannot give a definite answer about the origin of these oscillations.

## 6. Conclusions

When modeling high aspect ratio inclusions, ERS models are considered to be efficient replacements for conformal discretization approaches. The main shortcomings of these non-conformal approaches were demonstrated in this study and impair their general applicability. Although not reported here, the limitations reported in this study hold also under plane stress conditions and have been observed in three-dimensional simulations. These limitations are attributed to the continuity of field derivatives (*i.e.*, the matrix displacement gradients) across an inclusion.

Inaccuracies in the slip profile can become a limiting factor depending on the adopted material parameters. Inclusion stiffness, interface tangent stiffness, and inclusion cross sectional area are the model parameters which

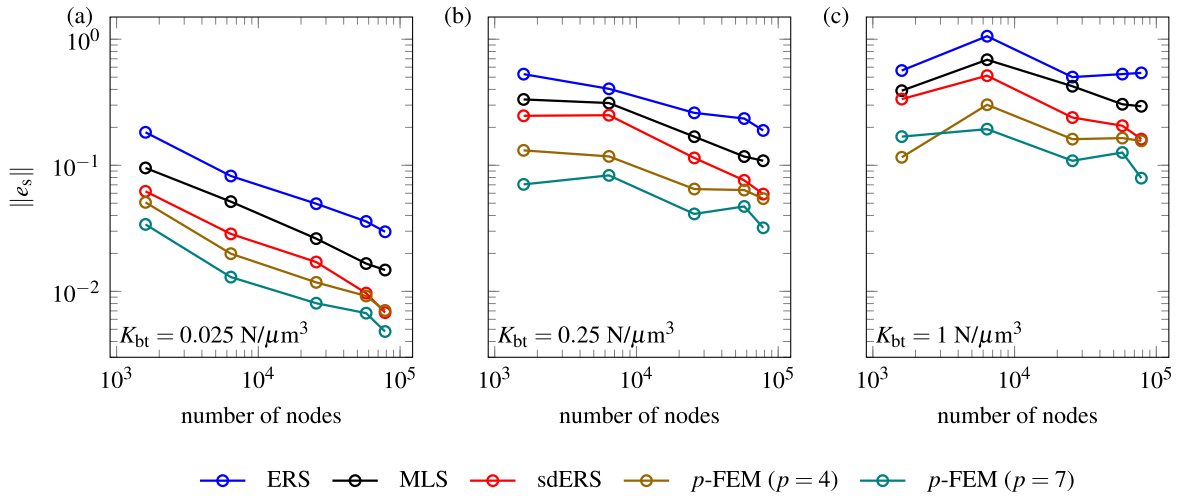


**Fig. 15.** Relative error in slip profiles for the single inclusion problem for different mesh densities and using various interface tangential stiffness values. The results are shown for the ERS model, the strain discontinuity enriched ERS (sdERS) model, the moving least squares (MLS) based model, and the  $p$ -version of the finite element based model ( $p$ -FEM with  $p$  equal to 4 and 7) using uniform Q4 discretizations.

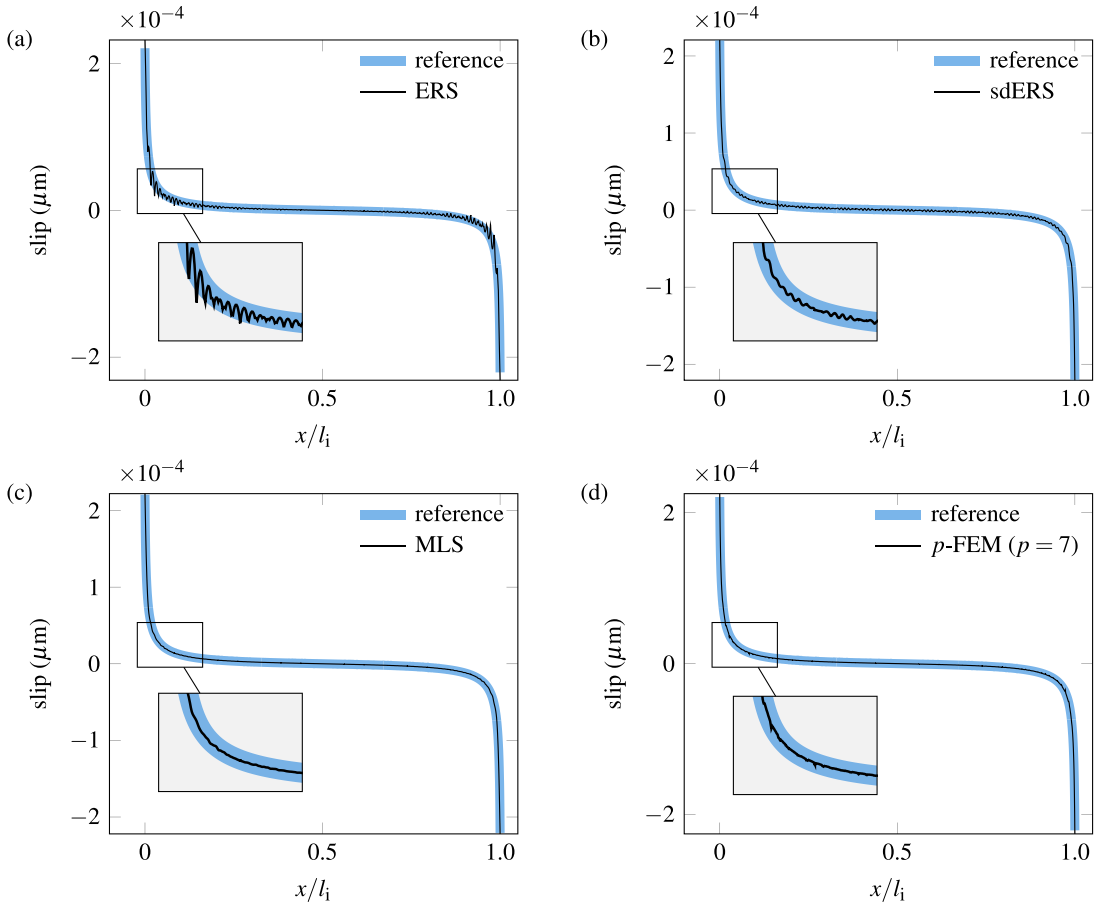


**Fig. 16.** Slip profiles for the single inclusion problem corresponding to the bond stiffness  $K_{bt} = 0.25 \text{ N}/\mu\text{m}^3$  obtained with the ERS model, the strain discontinuity enriched ERS (sdERS) model, moving least squares (MLS) based model, and  $p$ -version of the finite element based model ( $p$ -FEM with  $p = 7$ ). The results are shown using a uniform  $280 \times 280$  Q4 discretization and are accompanied by the reference slip profile obtained with a conformal FEM approach (uniform  $600 \times 600$  Q4 discretization).

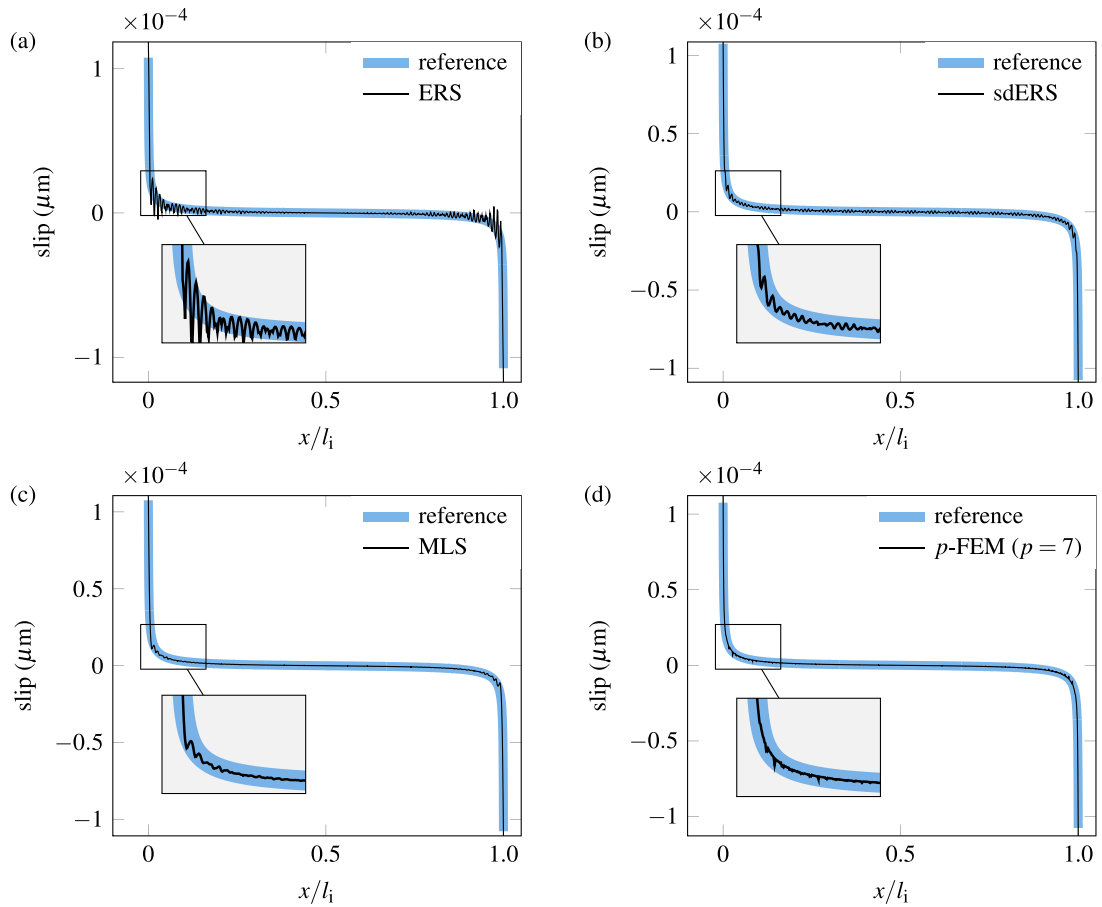


**Fig. 17.** Slip profiles for the single inclusion problem corresponding to the bond stiffness  $K_{bt} = 1 \text{ N}/\mu\text{m}^3$  obtained with the ERS model, the strain discontinuity enriched ERS (sdERS) model, moving least squares (MLS) based model, and  $p$ -version of the finite element based model ( $p$ -FEM with  $p = 7$ ). The results are shown using a uniform  $280 \times 280$  Q4 discretization and are accompanied by the reference slip profile obtained with a conformal FEM approach (uniform  $600 \times 600$  Q4 discretization).

were found to have the most adverse effect when relatively large values are used. To minimize these inaccuracies, one expensive treatment would be to use the proposed strain discontinuity enriched embedded reinforcement model with slip (sdERS). This model however requires the generation of a background integration mesh, an expensive task that is not advised in situations when an element is crossed by more than an inclusion. Besides, the complexity of a three-dimensional implementation does not make this model competitive. A relatively simpler strategy is the local elevation of the approximation order using either polynomial enrichments or the  $p$ -version of the finite element method. This strategy is preferred to the sdERS approach due to its simplicity. A more effective strategy might consist in improving the sdERS model with high order matrix displacement approximations but its generalization to higher dimensions is not straightforward.

## Acknowledgments

The research leading to these results has received funding from the European Research Council under the European Union's Seventh Framework Programme (FP7/2007-2013)/ERC Grant agreement n° 617972.

## References

- [1] H.R. Lusti, A.A. Gusev, Finite element predictions for the thermoelastic properties of nanotube reinforced polymers, *Modelling Simulation Mater. Sci. Eng.* 12 (3) (2004) S107.

- [2] S. Balakrishnan, D.W. Murray, Finite element prediction of reinforced concrete behavior. Structural Engineering Report No. 138, Department of Civil Engineering, The University of Alberta, July 1986.
- [3] J.M. Guedes, N. Kikuchi, Preprocessing and postprocessing for materials based on the homogenization method with adaptive finite element methods, *Comput. Methods Appl. Mech. Engrg.* 83 (2) (1990) 143–198.
- [4] E.A. Schauffert, G. Cusatis, Lattice discrete particle model for fiber-reinforced concrete. I: Theory, *J. Eng. Mech.* 138 (7) (2012) 826–833.
- [5] J.E. Bolander, S. Choi, S.R. Duddukuri, Fracture of fiber-reinforced cement composites: effects of fiber dispersion, *Int. J. Fract.* 154 (1–2) (2008) 73–86.
- [6] J.E. Bolander, S. Saito, Discrete modeling of short-fiber reinforcement in cementitious composites, *Adv. Cement Based Mater.* 6 (3) (1997) 76–86.
- [7] Y. Liu, N. Nishimura, Y. Otani, Large-scale modeling of carbon-nanotube composites by a fast multipole boundary element method, *Comput. Mater. Sci.* 34 (2) (2005) 173–187.
- [8] A. Ibrahimbegovic, A. Boulkertous, L. Davenne, D. Brancherie, Modelling of reinforced-concrete structures providing crack-spacing based on X-FEM, ED-FEM and novel operator split solution procedure, *Internat. J. Numer. Methods Engrg.* 83 (4) (2010) 452–481.
- [9] F.K.F. Radtke, A. Simone, L.J. Sluys, A computational model for failure analysis of fibre reinforced concrete with discrete treatment of fibres, *Eng. Fract. Mech.* 77 (4) (2010) 597–620.
- [10] A. Pros, P. Diez, C. Molins, Modeling steel fiber reinforced concrete: numerical immersed boundary approach and a phenomenological mesomodel for concrete-fiber interaction, *Internat. J. Numer. Methods Engrg.* 90 (1) (2012) 65–86.
- [11] G. Markou, M. Papadrakakis, An efficient generation method of embedded reinforcement in hexahedral elements for reinforced concrete simulations, *Adv. Eng. Softw.* 45 (1) (2012) 175–187.
- [12] V.M.C.F. Cunha, J.A.O. Barros, J.M. Sena-Cruz, A finite element model with discrete embedded elements for fibre reinforced composites, *Comput. Struct.* 94 (2012) 22–33.
- [13] C. Octávio, D. Dias-da-Costa, J. Alfaiate, E. Júlio, Modelling the behaviour of steel fibre reinforced concrete using a discrete strong discontinuity approach, *Eng. Fract. Mech.* 154 (2016) 12–23.
- [14] B. Mortazavi, M. Baniassadi, J. Bardon, S. Ahzi, Modeling of two-phase random composite materials by finite element, Mori–Tanaka and strong contrast methods, *Composites B* 45 (1) (2013) 1117–1125.
- [15] S. Soghrati, A. Nagarajan, B. Liang, Conforming to interface structured adaptive mesh refinement: new technique for the automated modeling of materials with complex microstructures, *Finite Elem. Anal. Des.* 125 (2017) 24–40.
- [16] N. Sheng, M.C. Boyce, D.M. Parks, G.C. Rutledge, J.I. Abes, R.E. Cohen, Multiscale micromechanical modeling of polymer/clay nanocomposites and the effective clay particle, *Polymer* 45 (2) (2004) 487–506.
- [17] K. Hbaieb, Q.X. Wang, Y.H.J. Chia, B. Cotterell, Modelling stiffness of polymer/clay nanocomposites, *Polymer* 48 (2007) 901–909.
- [18] J.M. Melenk, I. Babuška, The partition of unity finite element method: Basic theory and applications, *Comput. Methods Appl. Mech. Engrg.* 139 (1–4) (1996) 289–314.
- [19] N. Moës, M. Cloirec, P. Cartraud, J.F. Remacle, A computational approach to handle complex microstructure geometries, *Comput. Methods Appl. Mech. Engrg.* 192 (28–30) (2003) 3163–3177.
- [20] S. Omerović, T.-P. Fries, Conformal higher-order remeshing schemes for implicitly defined interface problems, *Internat. J. Numer. Methods Engrg.* 109 (6) (2017) 763–789.
- [21] S. Soghrati, A.M. Aragón, A.C. Duarte, P.H. Geubelle, An interface-enriched generalized FEM for problems with discontinuous gradient fields, *Internat. J. Numer. Methods Engrg.* 89 (8) (2012) 991–1008.
- [22] S. Soghrati, P.H. Geubelle, A 3D interface-enriched generalized finite element method for weakly discontinuous problems with complex internal geometries, *Comput. Methods Appl. Mech. Engrg.* 217–220 (2012) 46–57.
- [23] D.V. Phillips, O.C. Zienkiewicz, Finite element non-linear analysis of concrete structures, *Proc. Inst. Civ. Eng.* 61 (1) (1976) 59–88.
- [24] A.E. Elwi, T.M. Hrudey, Finite element model for curved embedded reinforcement, *J. Eng. Mech.* 115 (4) (1989) 740–754.
- [25] M.S.M. Sampaio, R.R. Paccola, H.B. Coda, Fully adherent fiber–matrix FEM formulation for geometrically nonlinear 2D solid analysis, *Finite Elem. Anal. Des.* 66 (2013) 12–25.
- [26] F. Barzegar, S. Maddipudi, Three-dimensional modeling of concrete structures. II: Reinforced concrete, *J. Struct. Eng.* 123 (10) (1997) 1347–1356.
- [27] H. Hartl, Development of a Continuum-Mechanics-Based Tool for 3D Finite Element Analysis of Reinforced Concrete Structures and Application to Problems of Soil-Structure Interaction (Doctoral thesis), Graz University of Technology, Austria, 2002.
- [28] J. Ninić, J. Stascheit, G. Meschke, Beam–solid contact formulation for finite element analysis of pile–soil interaction with arbitrary discretization, *Int. J. Numer. Anal. Methods Geomech.* 38 (14) (2014) 1453–1476.
- [29] F.K.F. Radtke, A. Simone, L.J. Sluys, A partition of unity finite element method for obtaining elastic properties of continua with embedded thin fibres, *Internat. J. Numer. Methods Engrg.* 84 (6) (2010) 708–732.
- [30] M.G. Pike, C. Oskay, XFEM modeling of short microfiber reinforced composites with cohesive interfaces, *Finite Elem. Anal. Des.* 106 (2015) 16–31.
- [31] M.G. Pike, C. Oskay, Three-dimensional modeling of short fiber-reinforced composites with extended finite-element method, *J. Eng. Mech.* 142 (11) (2016) 04016087.
- [32] D. Ngo, A.C. Scordelis, Finite element analysis of reinforced-concrete beams, *ACI J. Proc.* 64 (14) (1967) 152–163.
- [33] M. Goudarzi, A. Simone, Fiber neutrality in fiber-reinforced composites: Evidence from a computational study, *Int. J. Solids Struct.* 156–157 (2019) 14–28.
- [34] C.A.M. Duarte, J.T. Oden, An hp adaptive method using clouds, *Comput. Methods Appl. Mech. Engrg.* 139 (1996) 237–262.
- [35] C.A. Duarte, I. Babuška, J.T. Oden, Generalized finite element methods for three-dimensional structural mechanics problems, *Comput. Struct.* 77 (2000) 215–232.

- [36] R.L. Taylor, O.C. Zienkiewicz, E. Oñate, A hierarchical finite element method based on the partition of unity, *Comput. Methods Appl. Mech. Engrg.* 152 (1–2) (1998) 73–84.
- [37] P. Solin, K. Segeth, I. Dolezel, *Higher-Order Finite Element Methods*, CRC Press, 2003.
- [38] C.A.M. Duarte, J.T. Oden, Hp clouds – An hp meshless method, *Numer. Methods Partial Differential Equations* 12 (1996) 673–705.
- [39] A.M. Aragón, C.A. Duarte, P.H. Geubelle, Generalized finite element enrichment functions for discontinuous gradient fields, *Internat. J. Numer. Methods Engrg.* 82 (2010) 242–268.
- [40] B. Szabó, I. Babuška, *Introduction to Finite Element Analysis: Formulation, Verification and Validation*, John Wiley & Sons, 2011.
- [41] O. Van der Sluis, P.J.G. Schreurs, W.A.M. Brekelmans, H.E.H. Meijer, Overall behaviour of heterogeneous elastoviscoplastic materials: effect of microstructural modelling, *Mech. Mater.* 32 (8) (2000) 449–462.
- [42] O.C. Zienkiewicz, J.Z. Zhu, A simple error estimator and adaptive procedure for practical engineering analysis, *Internat. J. Numer. Methods Engrg.* 24 (2) (1987) 337–357.
- [43] O.C. Zienkiewicz, J.Z. Zhu, The superconvergent patch recovery and a posteriori error estimates. Part 1: The recovery technique, *Internat. J. Numer. Methods Engrg.* 33 (7) (1992) 1331–1364.
- [44] M.C. Rivara, Algorithms for refining triangular grids suitable for adaptive and multigrid techniques, *Internat. J. Numer. Methods Engrg.* 20 (4) (1984) 745–756.
- [45] J.C.J. Schellekens, R. De Borst, On the numerical integration of interface elements, *Internat. J. Numer. Methods Engrg.* 36 (1) (1993) 43–66.
- [46] P. Lancaster, K. Salkauskas, Surfaces generated by moving least squares methods, *Math. Comp.* 37 (155) (1981) 141–158.
- [47] D.H. McLain, Drawing contours from arbitrary data points, *Comput. J.* 17 (4) (1974) 318–324.
- [48] B. Nayroles, G. Touzot, P. Villon, Generalizing the finite element method: Diffuse approximation and diffuse elements, *Comput. Mech.* 10 (5) (1992) 307–318.
- [49] J. Dolbow, T. Belytschko, An introduction to programming the meshless Element Free Galerkin method, *Arch. Comput. Methods Eng.* 5 (3) (1998) 207–241.
- [50] B. Szabó, I. Babuška, *Finite Element Analysis*, John Wiley & Sons, 1991.